

CEERS Epoch 1 NIRC*am* Imaging: Reduction Methods and Simulations Enabling Early JWST Science Results

MICHAELA B. BAGLEY,¹ STEVEN L. FINKELSTEIN,¹ ANTON M. KOEKEMOER,² HENRY C. FERGUSON,²
PABLO ARRABAL HARO,³ MARK DICKINSON,³ JEYHAN S. KARTALTEPE,⁴ CASEY PAPOVICH,^{5,6} PABLO G. PÉREZ-GONZÁLEZ,⁷
NOR PIRZKAL,⁸ RACHEL S. SOMERVILLE,⁹ CHRISTOPHER N. A. WILLMER,¹⁰ GUANG YANG,^{11,12} L. Y. AARON YUNG,^{13,*}
ADRIANO FONTANA,¹⁴ ANDREA GRAZIAN,¹⁵ NORMAN A. GROGIN,² MICHAELA HIRSCHMANN,¹⁶ LISA J. KEWLEY,¹⁷
ALLISON KIRKPATRICK,¹⁸ DALE D. KOCEVSKI,¹⁹ JENNIFER M. LOTZ,²⁰ AUBREY MEDRANO,²¹ ALEXA M. MORALES,¹
LAURA PENTERICCI,¹⁴ SWARA RAVINDRANATH,² JONATHAN R. TRUMP,²² STEPHEN M. WILKINS,^{23,24}
ANTONELLO CALABRÒ,¹⁴ M. C. COOPER,²⁵ LUCA COSTANTIN,²⁶ ALEXANDER DE LA VEGA,²⁷ TAYLOR A. HUTCHISON,^{13,*}
RAY A. LUCAS,² ELIZABETH J. MCGRATH,¹⁹ XIN WANG,^{28,29} AND STIJN WUYTS³⁰

¹*Department of Astronomy, The University of Texas at Austin, Austin, TX, USA*

²*Space Telescope Science Institute, 3700 San Martin Drive, Baltimore, MD 21218, USA*

³*NSF's National Optical-Infrared Astronomy Research Laboratory, 950 N. Cherry Ave., Tucson, AZ 85719, USA*

⁴*Laboratory for Multiwavelength Astrophysics, School of Physics and Astronomy, Rochester Institute of Technology, 84 Lomb Memorial Drive, Rochester, NY 14623, USA*

⁵*Department of Physics and Astronomy, Texas A&M University, College Station, TX, 77843-4242 USA*

⁶*George P. and Cynthia Woods Mitchell Institute for Fundamental Physics and Astronomy, Texas A&M University, College Station, TX, 77843-4242 USA*

⁷*Centro de Astrobiología (CAB), CSIC-INTA, Ctra. de Ajalvir km 4, Torrejón de Ardoz, E-28850, Madrid, Spain*

⁸*ESA/AURA Space Telescope Science Institute*

⁹*Center for Computational Astrophysics, Flatiron Institute, 162 5th Avenue, New York, NY, 10010, USA*

¹⁰*Steward Observatory, University of Arizona, 933 N. Cherry Ave., Tucson, AZ, 85721, USA*

¹¹*Kapteyn Astronomical Institute, University of Groningen, P.O. Box 800, 9700 AV Groningen, The Netherlands*

¹²*SRON Netherlands Institute for Space Research, Postbus 800, 9700 AV Groningen, The Netherlands*

¹³*Astrophysics Science Division, NASA Goddard Space Flight Center, 8800 Greenbelt Rd, Greenbelt, MD 20771, USA*

¹⁴*INAF - Osservatorio Astronomico di Roma, via di Frascati 33, 00078 Monte Porzio Catone, Italy*

¹⁵*INAF-Osservatorio Astronomico di Padova, Vicolo dell'Osservatorio 5, I-35122, Padova, Italy*

¹⁶*Institute of Physics, Laboratory of Galaxy Evolution, Ecole Polytechnique Fédérale de Lausanne (EPFL), Observatoire de Sauverny, 1290 Versoix, Switzerland*

¹⁷*Center for Astrophysics — Harvard & Smithsonian, 60 Garden Street, Cambridge, MA 02138, USA*

¹⁸*Department of Physics and Astronomy, University of Kansas, Lawrence, KS 66045, USA*

¹⁹*Department of Physics and Astronomy, Colby College, Waterville, ME 04901, USA*

²⁰*Gemini Observatory/NSF's National Optical-Infrared Astronomy Research Laboratory, 950 N. Cherry Ave., Tucson, AZ 85719, USA*

²¹*University of Massachusetts Amherst, 710 North Pleasant Street, Amherst, MA 01003-9305, USA*

²²*Department of Physics, 196 Auditorium Road, Unit 3046, University of Connecticut, Storrs, CT 06269, USA*

²³*Astronomy Centre, University of Sussex, Falmer, Brighton BN1 9QH, UK*

²⁴*Institute of Space Sciences and Astronomy, University of Malta, Msida MSD 2080, Malta*

²⁵*Department of Physics & Astronomy, University of California, Irvine, 4129 Reines Hall, Irvine, CA 92697, USA*

²⁶*Centro de Astrobiología (CSIC-INTA), Ctra de Ajalvir km 4, Torrejón de Ardoz, 28850, Madrid, Spain*

²⁷*Department of Physics and Astronomy, University of California, 900 University Ave, Riverside, CA 92521, USA*

²⁸*School of Astronomy and Space Science, University of Chinese Academy of Sciences (UCAS), Beijing 100049, China*

²⁹*National Astronomical Observatories, Chinese Academy of Sciences, Beijing 100101, China*

³⁰*Department of Physics, University of Bath, Claverton Down, Bath BA2 7AY, UK*

ABSTRACT

We present the data release and data reduction process for the Epoch 1 NIRC*am* observations for the Cosmic Evolution Early Release Science Survey (CEERS). These data consist of NIRC*am* imaging in six broadband filters (F115W, F150W, F200W, F277W, F356W and F444W) and one medium

band filter (F410M) over four pointings, obtained in parallel with primary CEERS MIRI observations (Yang et al. in prep). We reduced the NIRCcam imaging with the *JWST* Calibration Pipeline, with custom modifications and reduction steps designed to address additional features and challenges with the data. Here we provide a detailed description of each step in our reduction and a discussion of future expected improvements. Our reduction process includes corrections for known pre-launch issues such as $1/f$ noise, as well as in-flight issues including snowballs, wisps, and astrometric alignment. Many of our custom reduction processes were first developed with pre-launch simulated NIRCcam imaging over the full 10 CEERS NIRCcam pointings. We present a description of the creation and reduction of this simulated dataset in the Appendix. We provide mosaics of the real images in a public release, as well as our reduction scripts with detailed explanations to allow users to reproduce our final data products. These represent one of the first official public datasets released from the Directors Discretionary Early Release Science (DD-ERS) program.

1. INTRODUCTION

The Directors Discretionary Early Release Science (DD-ERS) programs are providing the community with early and efficient demonstrations of the capabilities of *JWST* (Gardner et al. 2006). These public programs are designed to test multiple instruments and observing modes, and the teams have committed to sharing data products, tools and software, simulations and documentation before the *JWST* Cycle 2 call for proposals. The thirteen ERS programs cover a wide range of science topics and together have provided a wealth of information about early *JWST* performance and calibration.

Among these programs, the Cosmic Evolution Early Release Science Survey (CEERS; ERS 1345, PI: S Finkelstein) is obtaining imaging and spectroscopy of the Extended Groth Strip (EGS) *Hubble Space Telescope* (*HST*) legacy field with three *JWST* instruments and five coordinated parallel observing modes. The complete program involves imaging with the Near Infrared Camera (NIRCcam; Rieke et al. 2003, 2005; Beichman et al. 2012) short and long-wavelength channels in ten pointings, observed as coordinated parallels to primary observations with the Near Infrared Spectrograph (NIRSpec; Jakobsen et al. 2022) and the Mid-Infrared Instrument (MIRI; Rieke et al. 2015; Wright et al. 2015). Four of the ten pointings will be additionally covered by NIRCcam wide field slitless spectroscopy (WFSS) with MIRI imaging obtained in parallel. The complex CEERS survey layout results in multiple sets of overlapping observations, allowing for cross-instrument comparisons and enabling explorations of galaxies from $\sim 1 - 20\mu\text{m}$. The EGS field is additionally covered by an extensive set of multi-wavelength observations including imaging and spectroscopy with ground-based observatories, *HST*, and the *Spitzer Space Telescope*, from surveys including the Cosmic Assembly Near-infrared

Deep Extragalactic Legacy Survey (CANDELS; Grogin et al. 2011; Koekemoer et al. 2011), the MOSFIRE Deep Evolution Field Survey (MOSDEF; Kriek et al. 2015) and the DEEP2 Galaxy Redshift Survey (Newman et al. 2013).

The CEERS survey is optimized for the study of galaxies in the early universe ($z > 10$) and the processes of galaxy assembly and black hole growth for redshifts in the range $z \sim 1 - 10$. The NIRCcam and MIRI imaging will provide number counts of $z > 10$ candidate galaxies, robust stellar mass estimates for galaxies at $z > 4$, probes of dust-obscured star formation and super massive black hole accretion at $z \sim 1 - 3$, and detailed measurements of source morphologies. Multi-object spectroscopy with NIRSpec’s micro-shutter assembly (MSA) and NIRCcam’s wide field slitless spectroscopy (WFSS) will provide spectroscopic redshifts of sources at $z \sim 5 - 12$ through rest-ultraviolet (UV) and/or rest-optical emission lines, helping to constrain models of chemical evolution in the interstellar medium. The full details of the CEERS science goals and observing strategy will be presented in Finkelstein et al. (in prep).

In this paper, we present the CEERS team reduction of our NIRCcam imaging, providing a detailed description of our processing steps with the *JWST* Calibration Pipeline. Building on our team’s extensive experience from *HST*’s CANDELS program we have developed a number of custom processing steps and modifications to the Calibration Pipeline that improve on aspects such as imaging noise, detector features, alignment and global background modeling. Alongside this paper we will announce the first public release of our NIRCcam images, available for download at ceers.github.io/releases.html and on MAST as High Level Science Products via [10.17909/z7p0-8481](https://archive.stsci.edu/missions/jwst/10.17909/z7p0-8481). We include in this release scripts for downloading the raw NIRCcam imaging and processing it through the Calibration Pipeline along with all our custom scripts.

* NASA Postdoctoral Fellow

As part of our preparations for reducing the real NIRCam imaging, we created extensive simulations to replicate the CEERS observing strategy and expected detector noise and artifacts as closely as possible. These simulations help validate methods for source detection, photometry and morphological measurements, and were instrumental in building our strategies for working with the real NIRCam data. We have previously released our simulations as part of the CEERS Simulated Data Releases, which are available at the same website, and have also included NIRSpec MSA, NIRCam WFSS, and MIRI imaging simulations.

This paper is organized as follows. In Section 2, we describe the CEERS NIRCam observations obtained to date. We describe our image reduction in detail in Section 3, presented in three stages (Sections 3.1, 3.2, and 3.3). We discuss our custom corrections to remove snowballs (Section 3.1.1), wisps (Section 3.1.2) and $1/f$ noise (Section 3.1.3). In Section 3.3, we present the processing steps required to create combined mosaics, including astrometric alignment (Section 3.3.1), resampling (Section 3.3.2) and a custom background subtraction (Section 3.3.3). We discuss known issues present in our reduced data products in Section 4, and briefly summarize in Section 5. We also provide a detailed appendix, with a description of our released mosaic images (Appendix A), brief summaries of previous NIRCam data reduction versions that were used in early publications by the CEERS team (Appendix B), and a comprehensive discussion of the creation and reduction of our simulated NIRCam imaging (Appendices C and D). We express all magnitudes in the AB system (Oke & Gunn 1983) unless otherwise noted.

2. CEERS EPOCH 1 OBSERVATIONS

Due to the observability of the EGS field and the need for self-overlap of the CEERS observing modes, CEERS is schedulable in June or December, with a 180° position angle rotation between these times achieving similar survey layouts. Due to time constraints in the June 2022 observing window following telescope and instrument commissioning (EGS observability ends on July 1), the CEERS observations were split into two epochs. The first epoch was executed on 21 June, 2022. This involved CEERS pointings 1, 2, 3, and 6, which were observed with MIRI as the primary instrument and NIRCam in parallel. The remaining CEERS observations (six NIRSpec MSA+NIRCcam imaging pointings and four NIRCcam WFSS+MIRI imaging pointings) are scheduled for December 2022. We note that the current MIRI and NIRCcam observations do not overlap, but many of the MIRI pointings will have NIRCcam coverage once the rest

Table 1. CEERS Epoch 1 NIRCcam Observations

Filters		N Groups	Exptime
NIRCcam	MIRI		(s)
NIRCcam1 Field Center: 14:19:56.2 +52:58:38.8			
F115W+F277W	F770W	5	1546.1
F115W+F277W	F1000W	5	1546.1
F115W+F356W	F1280W	5	1546.1
F115W+F356W	F1500W	5	1546.1
F150W+F410M	F1800W	5	1546.1
F150W+F410M	F2100W	5	1546.1
F200W+F444W	F2100W	9	2834.5
NIRCcam2 Field Center: 14:19:34.8 +52:54:50.3			
F115W+F277W	F770W	5	1546.1
F115W+F277W	F1000W	5	1546.1
F115W+F356W	F1280W	5	1546.1
F115W+F356W	F1500W	5	1546.1
F150W+F410M	F1800W	5	1546.1
F150W+F410M	F2100W	5	1546.1
F200W+F444W	F2100W	9	2834.5
F200W+F444W ^a	F2100W	9	2834.5
NIRCcam3 Field Center: 14:19:12.7 +52:51:03.5			
F115W+F277W	F560W	9	2834.5
F115W+F356W	F770W	9	2834.5
F150W+F410M	F770W	9	2834.5
F200W+F444W	F770W	9	2834.5
NIRCcam6 Field Center: 14:19:25.2 +52:49:56.0			
F115W+F277W	F560W	9	2834.5
F115W+F356W	F770W	9	2834.5
F150W+F410M	F770W	9	2834.5
F200W+F444W	F770W	9	2834.5

^aThis observation was repeated at a slightly different PA on 28 June 2022 due to a problem with the MIRI observations, but is heavily affected by persistence, see Section 3.1.4 for details.

NOTE—All images are obtained in parallel with MIRI imaging as the primary instrument mode. All exposures use the MEDIUM8 readout pattern and a 3-point dither pattern determined by the MIRI PSF. The exposure times listed are the total including dithers.

of the survey observations are completed in December. In this paper, we focus on the CEERS Epoch 1 NIRCcam observations (hereafter referred to as NIRCcam1, NIRCcam2, NIRCcam3, and NIRCcam6) and reduction.

The NIRCcam instrument (Rieke et al. 2003, 2005; Beichman et al. 2012) consists of two modules, A and B,

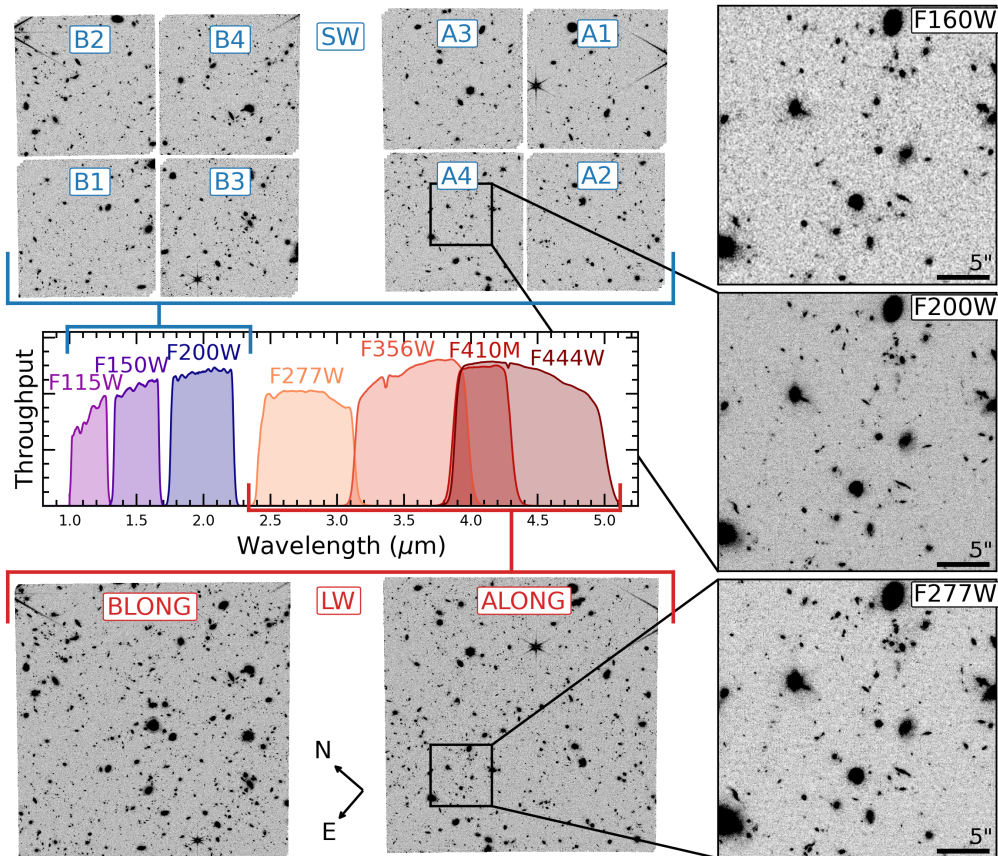


Figure 1. An illustration of the CEERS NIRCcam observations, using NIRCcam1 as an example. We show a SW (F200W) mosaic on the top left and a LW (F277W) mosaic on the bottom left. The SW and LW detectors are labeled in blue and red, respectively. The large module gap is visible in both mosaics, and the SW detector gaps are visible in the F200W mosaic. The CEERS filter throughput curves are plotted in the middle, with SW filters shown in purple-blue and LW filters in orange-red. Along the right edge, we show $29 \times 29''$ zoom-ins of the mosaic, with the same portion of the *HST* F160W mosaic displayed on top for reference. The black bars in the lower right corners of the zoom-in panels indicate a $5''$ scale.

each of which have a field-of-view covering $2.2' \times 2.2'$. The modules are separated by a $\sim 45''$ gap, making the total combined NIRCcam field-of-view ~ 9.7 arcmin 2 . Each module has four short wavelength (SW) detectors, A1-A4 and B1-B4, tuned for observations in the range $0.6 - 2.3\mu\text{m}$ and one long wavelength (LW) detector (ALONG and BLONG, $2.4 - 5\mu\text{m}$). Together, the SW detectors cover approximately the same area as the LW detectors, though they are separated by $\sim 5''$, leaving gaps in the SW mosaics that are not present in the LW mosaics. Observations in the SW and LW channels are obtained simultaneously. For CEERS Epoch 1, we have paired the following SW and LW filters together: F115W+F277W, F115W+F356W, F150W+F410M, and F200W+F444W. The filters are observed in this order to ensure that fading persistence from previous observations will not mimic a Lyman break in our images. In Figure 1, we show the seven NIRCcam filters as well as a SW (F200W) and LW (F277W) mosaic of NIRCcam1, with each individ-

ual detector labeled. The primary MIRI imaging is obtained with seven filters (see Table 1): F560W, F770W, F1000W, F1280W, F1500W, F1800W and F2100W. The CEERS MIRI imaging and reduction will be presented in Yang et al. (in prep).

We use a three-point dither pattern chosen to optimize the subpixel sampling and bad pixel mitigation for both NIRCcam and primary MIRI observations. As MIRI dithers are required to be $> 3\times$ the full width at half maximum (FWHM) of the MIRI point spread function (PSF), the dither steps are determined by the MIRI filter for each observation. Specifically, we use the dithers 3-POINT-MIRI-[filter]-WITH-NIRCcam, where *filter* is the primary MIRI filter. (The exception is for the observations with MIRI filter F560W, for which a custom dither pattern was not available and so we adopt that for F770W.) As a result, different dither step sizes are sometimes used for images in the same NIRCcam filter. However, as illustrated in Figure 1, most of the dithers are not large enough to cover the SW detector gaps. Our

NIRCam exposures use the MEDIUM8 readout pattern with either five or nine groups and one integration. The total exposure time is ~ 3000 seconds in each filter, with double the exposure time in F115W for added depth in the Ly α dropout filter for $z \gtrsim 9.5$ galaxies. Exposure times for each observation are listed in Table 1.

Finally, due to an on-board problem with MIRI pointing 2 at the time of observation, the last set of MIRI+NIRCam exposures in this pointing was re-observed on 28 June 2022 (see footnote *a* in Table 1). The original NIRCam observations were not affected. As a result, there is a second set of F200W+F444W imaging in this field at a slightly different position angle, providing added depth in these two filters. We note, however, that these additional images seem to be heavily affected by persistence (see Section 3.1.4 for a discussion). See Table 1 for details on Epoch 1 NIRCam observations and Finkelstein et al. (in prep) for more information on the CEERS Survey and observation specifications.

3. IMAGE REDUCTION

We process the raw images through the *JWST* Calibration Pipeline created and maintained by STScI (hereafter *JWST*), with custom steps and modifications informed from our work with the simulations described in Appendix D. The reduction described here and used to create our first public data release uses *JWST* version 1.7.2 and Calibration Reference Data System pipeline mapping (CRDS¹ pmap) 0989, which includes in-flight NIRCam dark, distortion, bad pixel mask, readnoise, and superbias reference files. It also includes the ground flats corrected for in-flight performance released on 18 August 2022 (pmap 0951) and the updated photometric calibration reference files² released on 4 October 2022. Pipeline mapping 0989 corresponds to the NIRCam instrument mapping (imap) 0232.

In the following sections we describe our image reduction steps in detail. We will also provide the parameter files for each pipeline step, custom Python routines for the additional corrections we have applied, and batch scripts for running all steps on all four NIRCam pointings on GitHub shortly following the data release. These scripts are summarized in Table 2 for reference. We invite the reader to use these scripts and parameter files to reproduce our reduction.

¹ jwst-crds.stsci.edu

² www.stsci.edu/contents/news/jwst/2022/an-improved-nircam-flux-calibration-is-now-available

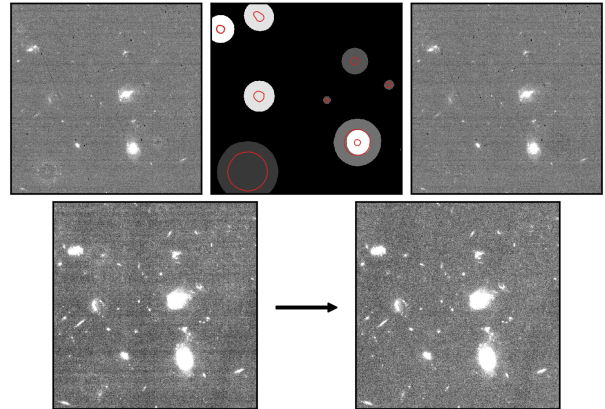


Figure 2. An example of the snowball correction. In the top row we show a portion of an F115W countrate map that includes several snowballs. The left image shows the output of the default *JWST*, where there is a particularly large snowball present in the lower left corner of the image. The middle shows the mask generated by identifying and growing the snowball footprints, where the red contours identify the original footprints. The snowballs are color-coded by the group in which they were detected, brighter snowballs were detected in later groups. The right panel shows the countrate map resulting from refitting the ramp with the updated snowball mask added to the *GROUPDQ* arrays. In the bottom row we show the portion of the F115W mosaic that corresponds to this region. In the left panel, the mosaic has been created without correcting for the snowballs in the individual exposures, while the right panel shows a mosaic that included this correction. The three CEERS dithers are not sufficient to compensate for the presence of snowballs. This additional correction is needed to remove them from the coadded mosaics. We note that the left panel also includes $1/f$ noise, which we discuss in Section 3.1.3.

3.1. Stage 1 – Detector-level corrections

Stage 1 of the *JWST* Calibration Pipeline performs detector-level corrections, many of which are common to all instruments and observing modes. The reduction steps involve initializing the data quality (DQ) arrays for flagging pixels; identifying saturated pixels; subtracting the superbias; using reference pixels to correct for readout noise; correcting pixels for non-linearity; subtracting the dark current; identifying cosmic rays as jumps in each pixel’s up-the-ramp signal; and calculating a linear fit to the unflagged ramp data to determine the average countrate per pixel. The end product of Stage 1 is a countrate image in units of counts/s. We adopt the default parameter values for these steps. We run the reduction steps of Stage 1 together with the snowball correction described in the following section (3.1.1), using the Python script `snowball_wrapper.py` described in the following section. For reference we also provide

Table 2. CEERS NIRC*am* v0.5 Reduction

Reduction Step	Script Name	Discussion in Text
Stage 1 + Snowball Correction	<code>snowball_wrapper.py</code>	Sections 3.1, 3.1.1
Wisp Subtraction	<code>wispsub.py</code>	Section 3.1.2
1/ <i>f</i> Noise Removal	<code>remstriping.py</code>	Section 3.1.3
Stage 2	<code>image2.1.7.2.asdf</code>	Section 3.2
SkyMatch + Outlier Detection	<code>image3_part1.asdf</code>	Section 3.3
Astrometric Alignment	<code>run_tweakreg.py</code>	Section 3.3.1
Individual Background Subtraction + Variance Map Rescaling	<code>skywcsvar.py</code>	Section 3.3.2
Mosaic Creation	<code>image3_nircam[pointing]_[chn].asdf^a</code>	Section 3.3.2
Mosaic background subtraction	<code>mosaic_background.py</code>	Section 3.3.3

^aWe use different parameter files for creating SW and LW mosaics, where the only difference is the input-to-output pixel size ratio. Here, `chn` refers to either the SW or LW channels.

the pipeline parameter file `detector1.1.7.2.asdf` with the equivalent set of default parameter values.

In the following subsections, we describe some features of the NIRC*am* images for which we have developed custom corrections. We refer the reader to Rigby et al. (2022) for more information on detector performance and some of these features that were discovered and characterized during commissioning.

3.1.1. Snowball Correction

“Snowballs” are large cosmic ray events that can affect hundreds of pixels and have a circular morphology on the NIRC*am* detectors. We see an average of $\sim 25 - 30$ snowballs per detector in a ~ 900 second exposure. The fluence of counts in the center of the snowballs is very high and can sometimes saturate the detector. The cosmic ray flagging step of JWST often successfully identifies and flags the central cores of these large cosmic rays, leaving the more diffuse wings of the snowballs present in the count rate maps output by Stage 1. The top left panel of Figure 2 shows an example of a countrate map containing multiple snowballs that were only partially removed by the pipeline.

We identify snowballs as large contiguous sets of pixels in the GROUPDQ arrays that have been flagged as jumps (`JUMP_DET`). We found it helpful to divide the snowballs into two tiers: large ones, which require a rather large mask to address the extended wings, and smaller ones, which do not require masking as much additional area. In order to separate snowballs from smaller cosmic ray impacts, we median filter the GROUPDQ arrays with separate two-dimensional tophat kernels with radii of 7 and 15 pixels to identify the smaller and larger snowballs, respectively. This filtering recovers extended groups of pixels that have an approximately circular footprint. We

also include in the snowball mask any saturated pixels that are within these big groups. We then grow the resulting snowball footprints via binary dilation and a two-stage tophat growing kernel with radii of 7 and 35 pixels. We add this updated snowball mask to the GROUPDQ array, and run the ramp-fitting step from JWST Stage 1. The flux in the affected pixels is determined by the remainder of the ramp, using the slope of the ramp excluding the newly-identified cosmic ray jump. The top middle panel of Figure 2 shows the DQ array for the count rate map in the left panel, with the original footprints of the snowballs identified with red contours. The top right panel shows the output countrate map that results from performing this snowball correction. In the bottom row, we show the portion of the mosaic that corresponds to the region displayed in the top row to demonstrate the effectiveness of this correction.

The snowball correction is performed with our Python script `snowball_wrapper.py`, that runs Stage 1 of the pipeline, saves the ramps from the first run of the ramp fitting step, identifies the snowballs and grows their footprint, flags them as cosmic rays, and then runs the ramp fitting step again to create a countrate map that excludes the flagged portions of the ramps.

We note that persistence from the saturated cores of very bright snowballs can show up in subsequent exposures. These are faint enough not to be rejected when the dithered images are combined. They can show up as single-band detections that look a lot like faint emission-line galaxies. For pure emission-line sources in WFSS exposures, it is important to inspect the individual exposures and their data-quality arrays.

3.1.2. Wisp Subtraction

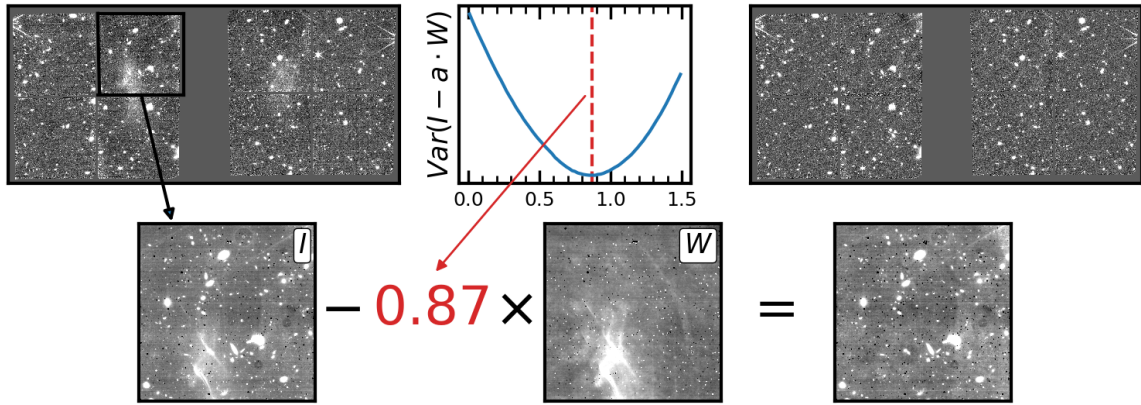


Figure 3. An illustration of our wisp subtraction process. The upper left panel shows the full extent of the wisps in an F200W mosaic of CEERS NIRCcam pointing 1. We then illustrate the process of fitting the wisp templates using one F200W image from detector B4 as an example. We minimize the variance of the wisp template W scaled by a factor a and subtracted from the image I in order to find the best-fitting a (0.87 in this case). The lower right panel shows a cleaned version of the F200W image where the wisp feature has been removed. The upper right panel shows the full F200W mosaic for this pointing once the wisps are subtracted from all affected input images. The three images in the bottom row have been smoothed by a Gaussian kernel with $\sigma = 2$ pixels for display purposes.

We next subtract the “wisp” features from the F150W and F200W images. Wisps are created from stray light reflected off the secondary mirror supports. They are visible on detectors A3, A4, B3 and B4, and are most prominent in F150W and F200W. The strength of the wisps depends on the source of the reflected light, and so the wisps can have a variable brightness from exposure to exposure. The top left panel of Figure 3 shows a version of the F200W mosaic for CEERS NIRCcam pointing 1 from which we have not subtracted the wisps as an example of the large scale structure of this feature. They extend across two detectors in each module.

The NIRCcam team has provided wisps templates constructed from images obtained by several NIRCcam commissioning and ERS programs observed early in Cycle 1. At the time of this writing, two sets of templates have been released, in July and August 2022. Both sets of templates are available on the *JWST* User Documentation page on Claws and Wisps³. We use the updated wisps templates released 26 August 2022, which are the result of reprocessing the original observations with updated processing steps and reference files, including a correction for the large-scale variations in the ground flats consistent with that introduced by pmap 0956.

We scale the templates to account for the variable brightness of the wisps feature and subtract them from the images in the following way. We first apply the flat field to each image to match the flat-fielded templates and to measure the wisps feature in the flattened images.

For each image, we perform a very “cold” source detection (i.e., a very high detection threshold of 5.5σ) with `PHOTUTILS` (Bradley et al. 2020) to identify and mask out large, bright sources in the image while avoiding the wisps feature itself. Next, we smooth the wisps template with a Gaussian kernel with $\sigma = 2$ pixels. For an array of coefficients a , we find the value that minimizes $\sigma_{MAD}^2(I - aW)$, where σ_{MAD} is the median absolute deviation, I is the flat-fielded masked image, and W is the smoothed wisps template. We find that in almost all cases, we need to scale the wisps template by a factor < 1 . We scale the original (unsmoothed) wisps template by a and subtract it from the original (unflatfielded and unmasked) image. We illustrate this process in Figure 3.

While this scaling does well at removing the large-scale feature, our wisps subtraction is still preliminary. The current wisps templates were produced with an updated but still early NIRCcam reduction. Additionally, in early Cycle 1 observations, the dithers were often small compared to the size of the sources observed. As a result, some ghost images of bright sources are present in some of the wisps templates and therefore become regions of oversubtraction (by $\sim 3 - 4\%$) in the CEERS images. We also note that we see some evidence for the presence of weak wisps in F115W, but as there are no templates available for this filter, we leave it uncorrected. The wisps templates will be improved throughout Cycle 1 with additional observations and updates to the NIRCcam reduction and reference files.

3.1.3. $1/f$ Noise Subtraction

Our final custom step on the countrate images is to measure and remove $1/f$ noise, which is correlated noise

³ The updated templates are packaged in `wisps_2022_08_26.tgz` available at jwst-docs.stsci.edu/jwst-near-infrared-camera/nircam-features-and-caveats/nircam-claws-and-wisps

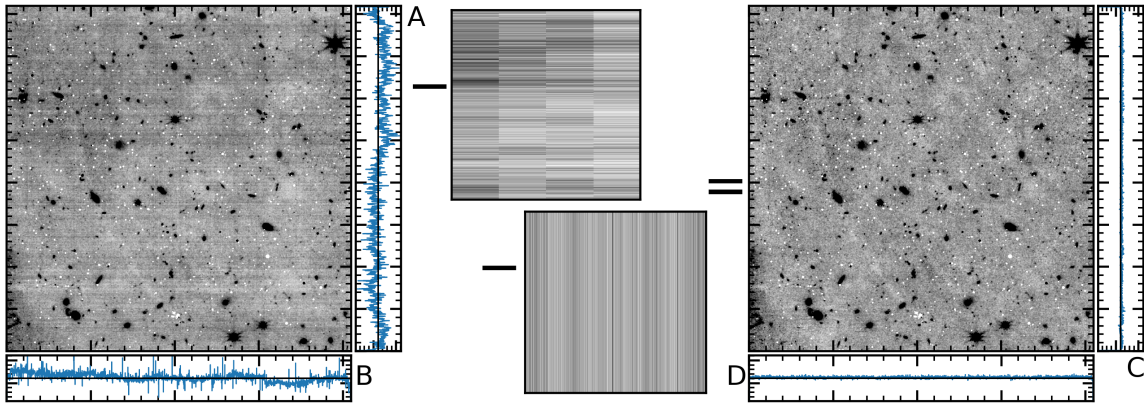


Figure 4. An illustration of our process for removing $1/f$ noise from countrate maps. The image on the left shows an input countrate map in F200W affected by $1/f$ noise. We show the median pixel value measured in the unmasked portions of each row (panel A) and column (B) in blue along the right and bottom edges, respectively, showing significant variation due to $1/f$ noise. The middle panels show the horizontal and vertical striping patterns that we identify using the unmasked portions of the image. The amplifier-dependent pattern is visible in the horizontal striping model. The image on the right shows the result of subtracting both models, where the right (C) and bottom (D) panels show that the noise in the image has been significantly reduced. All four panels displaying the median pixel values (A-D) are plotted with the same limits ± 0 . The countrate maps are flat-fielded and smoothed by a Gaussian kernel with $\sigma = 2$ pixels.

introduced in the images when the detectors are read out (Schlawin et al. 2020). The noise presents as horizontal and vertical striping patterns that vary from row to row and column to column. Ideally, this noise would be fit and removed during the reference pixel fitting or the up-the-ramp fitting of JWST, an update that may be included in future versions of the Calibration Pipeline. In the meantime, we perform our own correction for $1/f$ noise in each individual countrate map as follows.

As an additive effect, the noise pattern should be removed before applying the multiplicative flat field correction, yet the striping patterns are best measured on flat images. We therefore apply the flat field to the countrate maps for pattern measurement, but we subtract it from the original countrate images. We next mask all bad pixels (with a data quality flag value > 0) and source flux that is identified with PHOTUTILS using a tiered source detection method. This method consists of convolving the image with progressively smaller kernels and running a segmentation-style source detection at each step. In this way we are able to detect both large, extended sources and small, compact sources with detection parameters optimized for each source size. We use four tiers, with Gaussian kernels of $\sigma = 25, 15, 5$ and 2 pixels (on the original $0''.031/\text{pixel}$ and $0''.063/\text{pixel}$ scales for the SW and LW channels, respectively). These values were chosen after experimenting with several filter kernels to aggressively mask as much source flux as possible. Next we calculate a pedestal value for the sky background by fitting a Gaussian to the distribution of pixel values in the masked image.

We measure the striping pattern using a sigma-clipped (2σ) median along first rows and then columns. For the row correction (horizontal striping), we measure and remove the pattern amplifier-by-amplifier. In some images, especially in the SW filters, the difference from amplifier to amplifier can vary by $\sim 3 - 5\%$, and so this amplifier-dependent correction works better than using the median from the full row. However, in some cases, especially around bright or extended sources, a large number of pixels in a given amp-row are masked leaving too few to calculate a robust median. In these cases, we use the median of the entire row for the affected amp-row. The threshold used to determine the cutoff in number of masked pixels per amp-row varies from image to image to allow for the best pattern subtraction. We illustrate this amp-row and column subtraction in Figure 4.

This amp-by-amp approach works well for NIRCcam imaging, especially for fields like the EGS that are relatively sparsely populated (compared to a globular cluster, star field, or regions with high nebosity, for example, where a majority of pixels in individual amplifier rows will be masked). However, it is not a good approach for NIRCcam WFSS observations, where the length of a trace in the row grism is approximately the same size as an amplifier for some filters.

3.1.4. Additional Imaging in NIRCcam2

The observations of CEERS MIRI pointing 2 on 21 June 2022 encountered a problem writing data to disk, and one of the F2100W (with NIRCcam F200W+F444W in parallel) image sets was repeated on 28 June. See

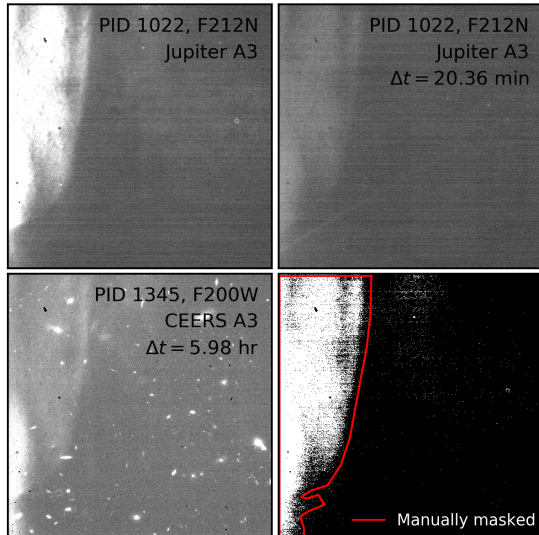


Figure 5. The persistence in the additional F200W imaging in NIRCAM2. The top row shows persistent or scattered light present in A3 images of commissioning program 1022, in which Jupiter was observed on detector A1. These two images are displayed with the same zscale stretch to highlight how the illumination pattern is fading with time. One of the CEERS F200W exposures obtained ~ 6 hours later is displayed in the lower left panel, where the same pattern is visible. We constructed a mask of pixels with elevated counts in both images from program 1022, shown in the lower right panel. We then manually masked the pixels within the red histogram, necessary to mask the fainter edges of the pattern that otherwise are present in the final mosaic. None of the other detectors contain clear signatures of persistence. Regardless, a future reduction will include a more careful treatment of persistence in these observations.

Yang et al. (in prep) for a full discussion of the effect on the MIRI images. The NIRCAM images from 21 June were not affected, and the repeated observations offer additional depth in F200W and F444W, though at a slightly different position angle. However, the repeat observations obtained on 28 June appear to suffer from significant persistence on SW detector A3.

We searched MAST for all NIRCAM observations obtained in the 24 hours before the NIRCAM2 repeat imaging. Program 1022 (PI: J Stansberry) observed Jupiter ~ 6 hours before the CEERS imaging. This commissioning program aimed to test the Fine Guidance Sensor (FGS) guiding near a bright planet as well as to characterize the scattered light in each instrument. There were two observations obtained with Jupiter on SW detector A1 (F212N) and LW detector ALONG (F322W2). In both cases, the same illumination pattern is present on SW detector A3 as that we see in the CEERS images. We show the calibrated (processed through pipeline Stages 1 and 2, flat-fielded and in units of MJy/sr) A3

detector images from program 1022 in the top two panels of Figure 5. The pattern is fainter in the second image, obtained 20.3 minutes after the first, indicating that the pattern is fading with time as expected for persistence. The feature on the detector A3 images may be scattered light from Jupiter imaged off-detector, or fading persistence from an earlier observation. (The program observed before 1022, and 8–10 hours before CEERS, is proprietary – GO 2473, PI: L Albert.) We note that neither the observations of Jupiter on detector A1 nor any of the LW images left persistence in the CEERS images.

We create a mask using the two A3 images from program 1022, identifying affected pixels as those with a flux >20 MJy/sr in the first exposure and >10 MJy/sr in the second exposure. These thresholds were found through trial and error to identify the persistent pattern and avoid flagging noise fluctuations. The lower right panel of Figure 5 shows the mask we created in this way, with flagged pixels in white. However, we found that this mask was not sufficient around the scattered light pattern. The wings of the pattern were still present in our F200W mosaics, and so we manually masked out a region around the affected area, shown as the red polygon in Figure 5. This method represents a preliminary approach to handling the persistence in this field. In future data reductions, we will create a more careful mask incorporating the CEERS images to identify the fading pattern. Here we have also created a mask for detector A3 only. In the future we will explore persistence on all detectors.

We apply the mask to the snowball-corrected count-rate maps by setting the image pixels to zero in the science extensions and setting their data quality (DQ) values to `DO_NOT_USE`. We then perform the corrections for wisps and $1/f$ noise as described above. We create three sets of mosaics in F200W and F444W for NIRCAM2: one containing just the original imaging, one with just the repeated imaging, and one including both sets of imaging.

3.2. Stage 2 – Individual Image Calibrations

Stage 2 of *JWST* involves steps such as flat-fielding the data and applying the flux calibration that converts the images from counts/s to MJy/sr. We adopt the default values for these pipeline steps. We note that the NIRCAM flats used are ground flats that have been corrected for an illumination gradient using in-flight observations. Additionally, the flux calibration is based on observations of three standard stars (PIDs 1536, 1537 and 1538) that have been observed across all ten NIRCAM detectors. It builds on the work of several teams, including the Resolved Stellar Populations ERS program (PID

1334, PI D. Weisz) observations of the globular cluster M92 (Boyer et al. 2022; Nardiello et al. 2022), zeropoints derived by G. Brammer⁴, and early absolute flux zeropoints from the NIRCcam team (M. Rieke, private communication). Both the flat fields and the flux calibration tables are important reference files that will continue to be updated throughout Cycle 1.

3.3. Stage 3 – Ensemble Processing

Stage 3 performs ensemble reduction steps, where the output product is a single mosaic per filter combining all images and dithers. These steps include astrometric alignment, background matching, outlier detection, and resampling the images onto a common output grid. We break this stage up into individual steps, first applying a customized astrometric correction, then running the `OutlierDetection` step of `JWST` Stage 3 with the default parameter values. Then we background-subtract each individual file and perform two additional corrections on the variance arrays before resampling the images into one combined mosaic per filter. Finally, we perform a custom background subtraction of the mosaics to remove any residual background. In the following subsections, we describe these customized processing steps.

3.3.1. Astrometric Alignment

We perform an astrometric calibration using a modified version of the `JWST TWEAKREG` routine, with the modifications primarily aimed at exposing more fitting parameters and being able to input our own catalogs (similar modifications are also in progress in the official STScI pipeline). The `TWEAKREG` routine calculates the transformation needed to align images to an absolute WCS frame. It does this by comparing the source positions detected in each input image with their matches in a reference catalog. With our modified version of this step, we create a `SOURCE EXTRACTOR` (Bertin & Arnouts 1996) catalog for each individual input image, providing improved source detection, deblending and centroiding over the internal `TWEAKREG` source identification. We also use a custom reference catalog derived from a *HST* F160W 0'03/pixel mosaic⁵ in the EGS field with astrometry tied to Gaia-EDR3 (see Koekemoer et al. 2011, for further details on the methods for image processing and mosaic creation). In both cases we use the `SOURCE EXTRACTOR` windowed coordinates for improved centroiding, which especially improves positions for the compact sources that we primarily use for our alignment.

We calculate both a relative and absolute astrometric correction. The images are first aligned relative to each other, where shifts in x and y are determined between images of the same detector. This step accounts for uncertainties in the guide star alignment and pointing accuracy during dithering. The RMS of this relative astrometry is $\sim 3 - 6$ mas per source. The images are then aligned to the *HST* F160W reference catalog, allowing for xy shifts and rotations. In the LW images we also allow for a scaling factor to account for any additional distortion across the larger detectors, though we note that the calculated deviations from a unity scaling factor are small ($\sim 1 \times 10^{-5}$). The RMS of this absolute alignment (WFC3-to-NIRCcam) is $\sim 12 - 15$ mas, and is driven by the larger F160W PSF. The RMS of the alignment between NIRCcam images in different filters (NIRCcam-to-NIRCcam) is $\sim 5 - 10$ mas, with SW images at the smaller end and LW images at the larger end of that range. Figure 6 illustrates the quality of the astrometry in F200W and F277W and shows both the *HST*-to-NIRCcam and NIRCcam-to-NIRCcam alignment.

In summary, for all four NIRCcam fields (1, 2, 3, and 6), for all filters and all detectors in both modules, the RMS astrometric alignment quality is generally $\sim 5 - 10$ mas per source between NIRCcam filters (SW - LW), and $\sim 12 - 15$ mas per source relative to the absolute frame defined by the *HST* F160W mosaic. There is however one exception to this: for NIRCcam pointing 3, specifically for a $\sim 1'$ region in the quadrant of the mosaic mostly covered by the B2 detector, the astrometric offsets relative to the *HST* F160W mosaic are larger, $\sim 0''.05$ (or about one-fifth of the $0''.23$ *HST* F160W mosaic PSF in this mosaic⁶). These offsets are also present in this region of the LW BLONG module, suggesting that it is not an alignment problem with a specific SW detector. After detailed examination of the relevant datasets, a possibility is that the *HST* F160W exposures for the particular visit in that part of the mosaic were affected by a low-level guidestar tracking issue, at the sub-PSF level ($\sim 1/5$ of a PSF), which can occasionally occur and is not always revealed by the guidestar telemetry keywords in the image headers. Since these residuals are small compared to the size of the F160W PSF, they are unlikely to significantly affect the overall *HST*-NIRCcam photometry since our apertures are generally substan-

⁴ github.com/gbrammer/grizli/pull/107

⁵ ceers.github.io/hdr1.html

⁶ Note that, while the FWHM of the optical PSF of *HST* is $0''.151$ for F160W, this is subsequently convolved by: (1) the WFC3/IR detector pixel size when the field is imaged, (2) by a factor `pixfrac=0.8` times the WFC3/IR detector pixel size, and (3) by the mosaic pixel size, therefore yielding a final PSF FWHM of $\sim 0''.23$ in the F160W mosaic, which is standard for this instrument.

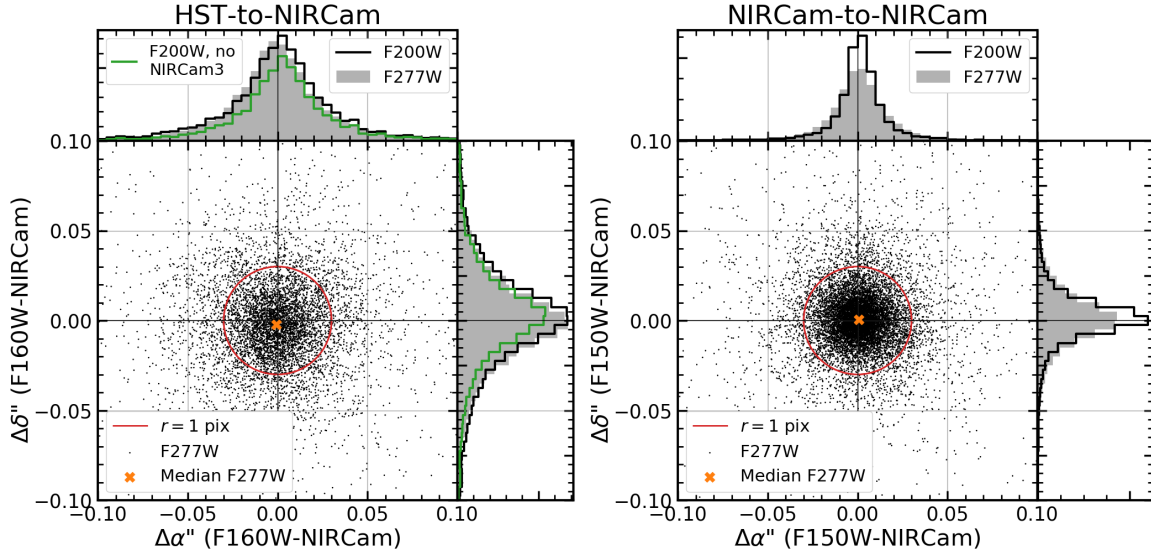


Figure 6. Diagnostic plots of the CEERS NIRCAM astrometric alignment. In the left panel we show the offsets for sources detected in all four pointings when compared with their positions in the *HST* F160W mosaic. The right panels show astrometric offsets compared with positions in the NIRCAM F150W mosaic. The black points in the scatter plots show the offsets for source positions in the F277W images, and the orange ‘x’ indicates the median astrometric offset. The filled histograms show the distribution of offsets in right ascension and declination for F277W source positions, and the empty histogram shows the same for source positions in the F200W images. We show both a SW and LW filter to indicate the quality of the astrometry in both channels. The red circles have a radius of $0''.03$, or one pixel in the output mosaics. Both cases show a median offset consistent with 0, and an RMS scatter less than one pixel. The RMS of the *HST*-to-NIRCAM alignment is $\sim 12 - 15$ mas while that of the NIRCAM-to-NIRCAM alignment is $\sim 5 - 10$ mas, generally smaller for the SW and larger for the LW filters. In the left panel, the green histogram indicates the F200W distribution excluding NIRCAM3, the field that exhibits larger offsets relative to *HST* (see the text for details). The F277W distribution excluding NIRCAM3 is very similar.

tially larger than the *HST* PSF. We therefore followed a different process for aligning this NIRCAM pointing. We first aligned F277W to F160W, excluding all sources in the upper left quadrant of detector BLONG from the fit. We then used F277W rather than F160W as the reference catalog for all other filters in this pointing. The RMS of the alignment is still $\sim 3 - 6$ mas (relative) and $\sim 5 - 10$ mas (absolute NIRCAM-to-F277W).

3.3.2. Mosaic Creation

Before combining individual exposures into mosaics, we perform three additional corrections to the calibrated images. First, we subtract a pedestal value in MJy/sr from each exposure. This step is necessary because the `SkyMatch` routine of `JWST` does not successfully match the background across all detectors, likely because the small dithers result in little to no overlap between detectors. In order to calculate the background, we mask bad pixels and source flux using the tiered masks created for each image in Section 3.1.3. We then fit a Gaussian to the distribution of unmasked, sigma-clipped pixel fluxes and take the position of the peak as the image pedestal. This single value is subtracted from each image, and the headers are updated to reflect this value. Second, we calculate the sky variance in each

background-subtracted image. To do this, we mask sources in four tiers, as described in Section 3.3.3. We then block-sum the image in units of 7×7 pixels and use `astropy`’s `biweight_midvariance` to make a robust estimate of the variance in blocks that have had no pixels masked. We estimate the equivalent per-pixel variance by dividing by the number of pixels per block (49). We then scale the readnoise variance array (`VAR_RNOISE`) to reproduce this value. Because `VAR_RNOISE` is used to compute the inverse variance that is used as weighting during the drizzle process, this ensures that the resulting error arrays do a good job of predicting the RMS sky fluctuations (when estimated over large enough scales to avoid the pixel-to-pixel correlations introduced by drizzling).

Third, we make one final correction to the variance arrays to ensure that bad pixels are properly flagged. With our simulated mosaics (see Appendix D.4), we found that some known bad pixels had values of exactly zero in the variance arrays. When the dithered images were co-added, these areas in the output error array had relatively low RMS compared with the average. In these areas, the input error array with the missing data or bad pixel did not contribute to the RMS of the affected pixel. As a result, there were ‘holes’ in the output er-

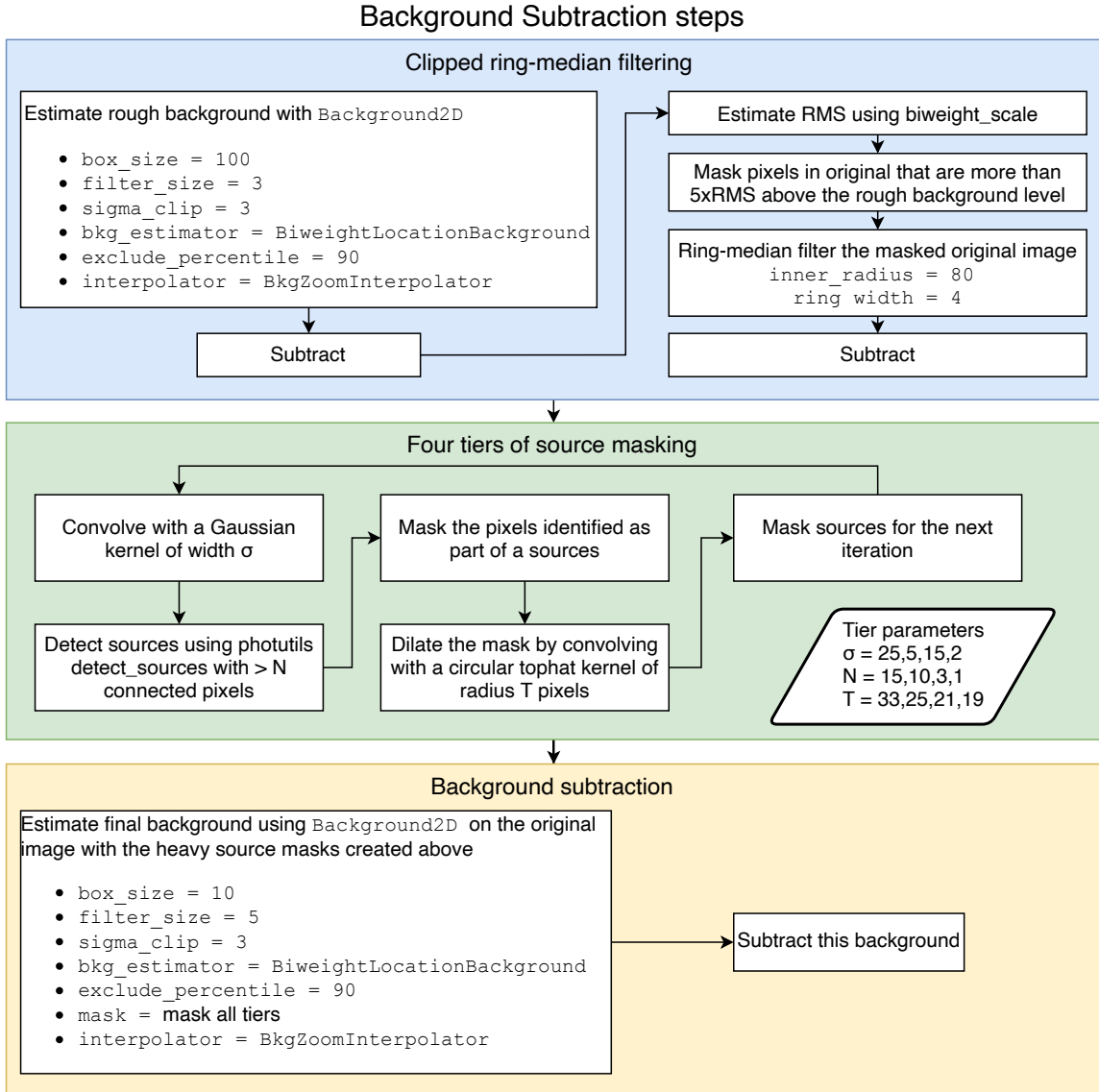


Figure 7. Steps for subtracting background from the co-added images.

ror arrays in sets of three, matching our three dithers. Spurious source detections were more prevalent in these areas because the RMS used for detection was low. For each individual image, we therefore replace any pixels that are exactly zero in the three variance arrays with values of infinity (`numpy.inf`). This correction ensures that the affected pixels are correctly down-weighted in the drizzling.

We create individual mosaics for each pointing using the Stage 3 routine `Resample`, which uses the drizzle algorithm with an inverse variance map weighting (Fruchter & Hook 2002; Casertano et al. 2000) to combine images into a single distortion-free image. The output mosaics are drizzled onto a common WCS with the same tangent point as the *HST* mosaics we have created in this field (see footnote 5). All *HST* and NIRC*am* mo-

saics are therefore pixel-aligned across all filters. The mosaics have pixel scales of $0''.03/\text{pixel}$, and we chose not to shrink the input NIRC*am* pixels when drizzling (i.e., `pixfrac = 1`). This larger `pixfrac` is preferred for CEERS because the majority of the mosaic is covered by at most three exposures. The output pixel scale is only slightly smaller than the original scale in the SW channel ($0''.031/\text{pixel}$) and just over two times smaller than that of the LW channel ($0''.063$). We discuss tests to evaluate the optimal drizzle parameters in Appendix D.4. The choice of `pixfrac` leads to increased pixel correlations in the output image, which we discuss in Section 4 and have not yet addressed in our mosaics.

These individual mosaics are included in our data release and the files and extensions are described in Appendix A. We also created a set of combined, Epoch

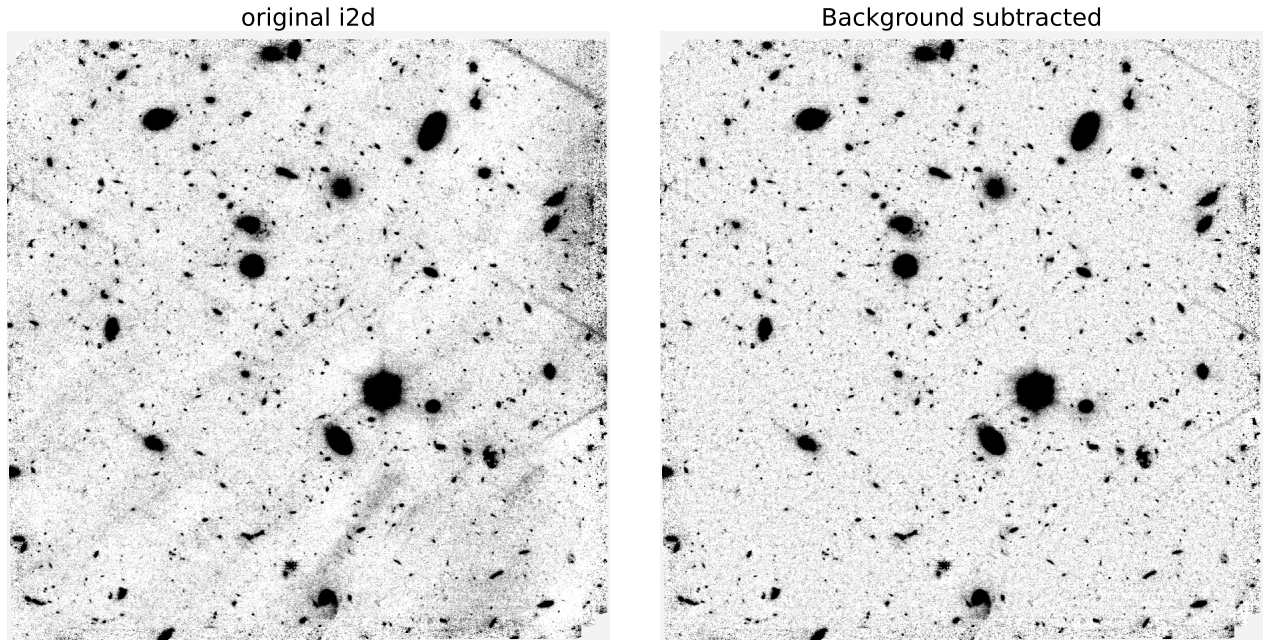


Figure 8. Example of background removal for a single detector in the F200W of CEERS field 1. The image on the left is the co-added image before background subtraction. The image on the right has had the fluctuating background removed as described in the text.

1 mosaics that include all four pointings. Constructing these Epoch 1 mosaics requires considerable memory (~ 600 GB, depending on the filter), and so we use the Frontera computing system at the Texas Advanced Computing Center (TACC). Frontera provides a set of large memory nodes that offer 2.1 TB of memory each with the option to link multiple nodes. A color image of the Epoch 1 mosaic including all seven filters is displayed in Figure 10.

3.3.3. Background Subtraction

Finally, we estimate and subtract any remaining background in the mosaics using a custom Python script that efficiently masks source flux before fitting the unmasked pixels with a two-dimensional model. The steps are outlined in Figure 7. The first step involves taking out large-scale fluctuations, masking bright pixels in the residual, and then running a large ring-median filter across that image to create the first good estimate of the background. The inner ring radius is $2.4''$ so this step preserves the wings of all but the largest galaxies in the image. This step creates background that is flat enough on large scales to permit us to mask sources above a fixed threshold without any perceptible gradients in source size and density due to large-scale changes in the background. We mask four tiers of sources, with tier number 1 intended to mask the most extended galaxies, moving progressively to the smallest galaxies at tier number 4. This is achieved by convolving the image with four dif-

ferent widths of Gaussians, and masking areas with a minimum number N of connected pixels above a fixed threshold of 1.5σ . These masks are then grown by dilating them with a circular tophat kernel with different kernel radii for each tier. We construct a source mask for each filter, including the pixel-aligned images in six available *HST* filters (F606W, F814W, F105W, F125W, F140W and F160W). We merge all 13 separate masks into one, which is used to mask source flux in all filters. In this way we can exclude flux from sources that may be just below the detection threshold in some filters but not others.

We then measure the background in the unmasked regions using the `PHOTUTILS Background2D` class. We use the `biweight_location` estimator to robustly calculate the average background in sigma-clipped boxes of 10×10 pixels in a grid across the image. The resulting low-resolution gridded background model is then median-filtered over 5×5 adjacent boxes, and the `BkgZoomInterpolator` algorithm is used to interpolate the filtered array and construct a smooth background model.

A “before and after” example of background removal is shown in Figure 8. Any estimation of background requires decisions about what is “source” and what is “background.” The procedure outlined above does a very good job of removing residual wisps and other artifacts in the NIRCcam images, while preserving the wings of most of the galaxies of interest. However, it does

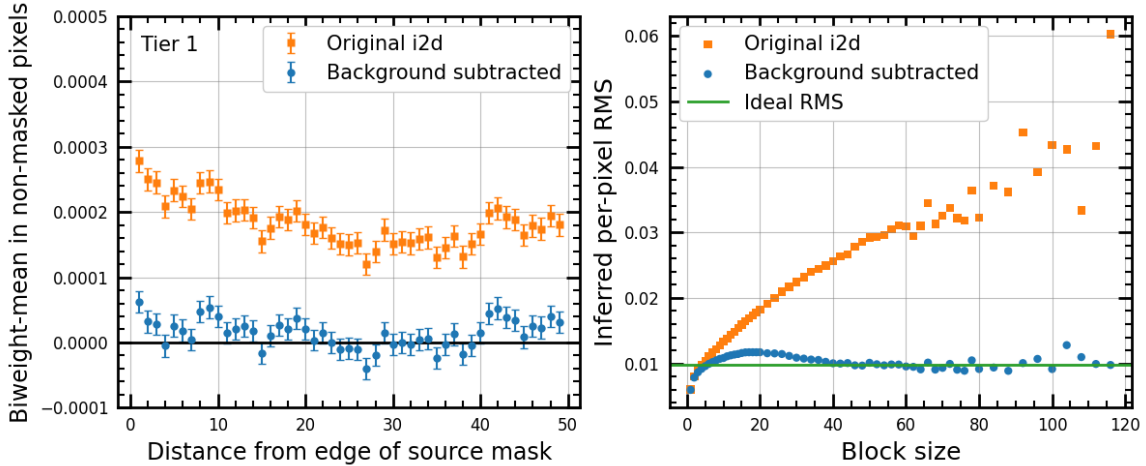


Figure 9. *Left:* Sky background around the borders of tier 1 of the source mask. Tier 1 has the largest convolution kernel, and therefore masks the most extended sources. The diagram here shows the background (in MJy/sr) in unmasked pixels beyond the boundaries of the galaxies in this mask, as a function of distance to the closest masked pixel. One can see the overall elevated background level in the points from the original i2d file. There is a slight gradient toward brighter pixels closer to the boundaries of the masks, as expected from the faint extended wings of galaxies. The blue points show that the typical background is zero, and that wings of the galaxies have been slightly suppressed. *Right:* Statistics as a function of scale before and after background removal in the F200W image of NIRCcam1. For each block size, the image has been block summed in boxes of $N \times N$ pixels. The variance is then computed for blocks that had no pixels masked during the background estimation (i.e. these are our best effort at source-free regions of the image). The equivalent per-pixel RMS from this estimate is $\sqrt{\text{var}}/N$. The image co-addition suppresses the pixel-to-pixel RMS on scales of a few pixels. On larger scales, the equivalent per-pixel RMS continues to grow in the original image due to the various non-uniformities. Some of these non-uniformities are from scattered light, but the procedure also suppresses the extended wings of bright galaxies. The fluctuations are suppressed on scales of more than about 40 pixels by the background-subtraction procedure. The remaining fluctuations on intermediate scales are due to the wings of galaxies and to galaxies below the detection threshold. The green line shows the ideal RMS expected if the sky fluctuations were due purely to photon counting statistics. This helps to confirm that the procedure has done an excellent job of removing large-scale non-uniformities in the image.

suppress the wings of bright galaxies (intentionally) to enable the detection of faint neighbors.

To assess the background subtraction, we examined the stacked flux in pixels as a function of distance from the edge of the four separate tiers of masks. In most bands, for most tiers, there is very little “spillage” of galaxy flux into the pixels that were used to estimate the background. This spillage is impossible to avoid entirely. It is at a low enough level that we do not think the wings of galaxies that are above our detection threshold are significantly biasing the large-scale background estimation. In the left panel of Figure 9 we show an example for F200W in one of our fields.

On large scales, one would like to see the RMS of the background approach the RMS expected from a completely flat image affected only by the counting statistics of the incoming signal. The right panel of Figure 9 shows the per-pixel RMS that is inferred from measuring the RMS in source-free (i.e. unmasked) regions of a F200W image, when block summed over successively larger block sizes and then rescaled back to the per-pixel RMS. On small scales, the RMS is suppressed in the combined images because the drizzling procedure intro-

duces a correlation between pixels. On medium scales, the residual wings of galaxies – which are impossible to remove entirely – slightly boost the RMS. The RMS approaches the ideal on larger scales, albeit with scatter in this measurement because there are very few blocks of 60×60 pixels and above that are entirely source free.

3.3.4. Field Depths

In Table 3, we present the 5σ limiting magnitudes in each filter and pointing. These depths are measured on our background-subtracted mosaics in circular apertures with radius $r = 0.1''$, and scaled to an empirical estimate of the noise in the image as described by Finkelstein et al. (2022, in prep). Briefly, apertures ranging in size from $r = 0.05''$ to $r = 1.5''$ are placed across each image, avoiding source flux and bad pixels. A robust estimate of the 1σ noise is calculated in each aperture, and following the examples of Papovich et al. (2016), Bagley et al. (2022) and Finkelstein et al. (2022a, see also Labbé et al. 2003; Blanc et al. 2008; Whitaker et al. 2011), a second order polynomial is fit to the noise as a function of aperture size. We use this function to estimate the noise in a $r = 0.1''$ aperture. Using stacked PSFs in each filter,

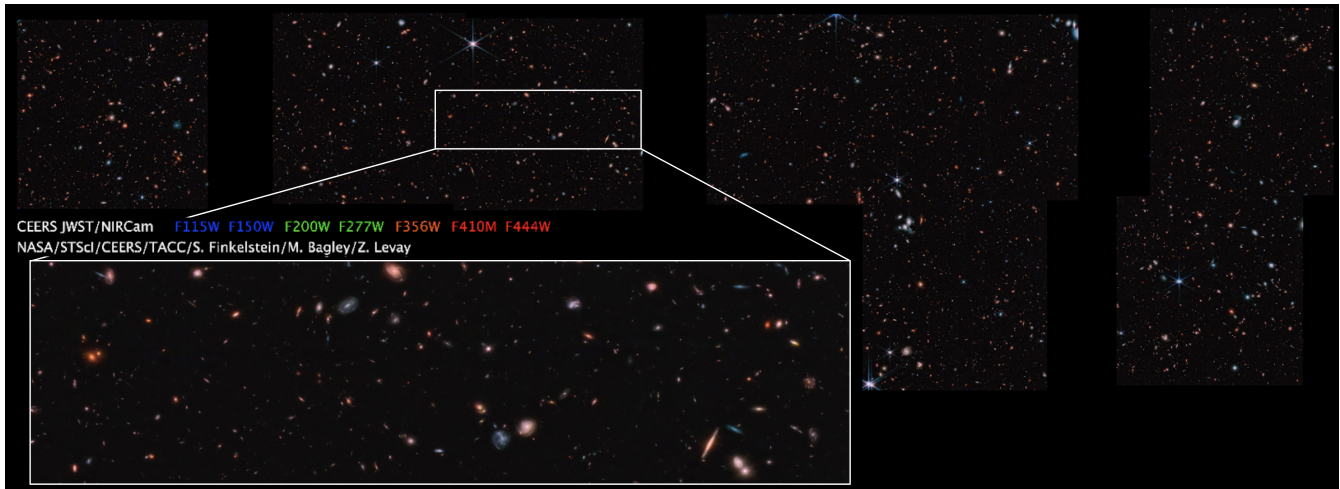


Figure 10. A seven color image of the CEERS Epoch 1 NIRCAM imaging. These images were reduced at the Texas Advanced Computing Center and colored by Zoltan Levay. High-resolution versions of these images and related information is available at ceers.github.io/ceers-first-images-release.html.

we then measure the fraction of the total flux that is enclosed in an aperture of this size and correct the noise estimate by this amount. See Finkelstein et al. (2022, in prep) for a full description of each step in this process. The 5σ depths for each pointing and filter are listed in Table 3.

3.3.5. Flux Calibration

As mentioned in Section 3.2, the CRDS pmap we use (0989) for our NIRCAM reduction includes updated photometric calibration reference files with zeropoints derived from early observations of three standard stars. Due to the nature of the CEERS observing strategy, the NIRCAM dithers are not large enough to observe a given source across multiple detectors, and so we do not have a direct test of detector-to-detector zeropoints. We therefore explore the relative photometric calibration between detectors with two methods, which we describe below.

For the first method, we measured aperture photometry on NIRCAM, *HST*/WFC3, and *Spitzer*/IRAC data for galaxies with $m < 24$ using Kron (1980) apertures. We compared the NIRCAM F115W filter to WFC3/F125W and F150W to F160W, after first matching the PSFs. We note that the passbands of these two pairs of filters are not exactly the same, preventing us from using this method to obtain an absolute photometric calibration. Moreover, the derivation of absolute zeropoints is challenging with extended sources due to uncertainties in aperture corrections, making it difficult to separate the color-dependent correction for missing source wings from the flux calibration. Yet the approach of comparing NIRCAM, WFC3 and IRAC fluxes in PSF-matched images should be robust for estimating relative

Table 3. NIRCAM Pointing 5σ Depths

Filter	NIRCAM1	NIRCAM2	NIRCAM3	NIRCAM6
F115W	29.08	29.10	29.21	29.21
F150W	28.96	28.94	29.05	29.04
F200W	29.17	29.16	29.21	29.16
F277W	29.16	29.20	29.22	29.19
F356W	29.14	29.17	29.18	29.18
F410M	28.37	28.35	28.41	28.40
F444W	28.57	28.58	28.58	28.58
F606W	28.62	28.62	28.62	28.62
F814W	28.30	28.30	28.30	28.30
F105W	...	27.11	27.11	27.11
F125W	27.31	27.31	27.31	27.31
F140W	26.67	26.67	26.67	26.67
F160W	27.37	27.37	27.37	27.37

NOTE—Depths are measured for point sources in $r = 0.1''$ circular apertures and corrected to total flux using the flux measured for a stacked PSF within that aperture. The depths for NIRCAM2 reported here are for the first set of observations only (obtained 21 June 2022) and do not include the additional imaging in F200W and F444W. All values are AB magnitudes. The depths in the *HST* filters are measured across the full EGS mosaics, and so have the same reported values here for each individual NIRCAM pointing. There is no WFC3 F105W coverage for NIRCAM1.

calibrations between detectors provided enough sources are used.

We use a second method for F200W, F277W, and F410M, for which there are no direct imaging data with comparable depth and spatial resolution available.

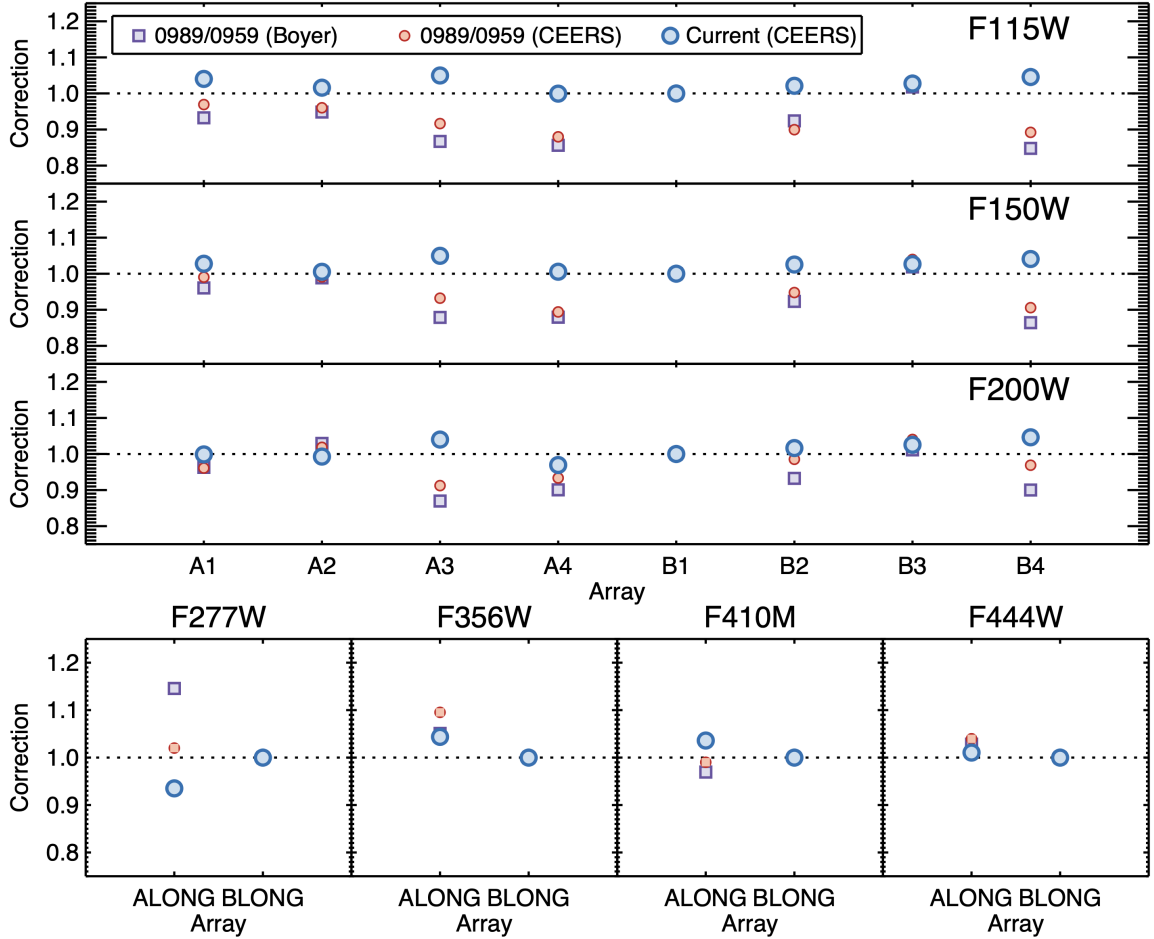


Figure 11. Evaluation of the relative detector-to-detector photometric calibration for the CEERS NIRCcam data. Squares show the relative multiplicative offsets with respect to the B1 (for SW) and B5 (for LW) detectors released in pmap-0989, which were calculated with data calibrated with pmap-0959 for an A-type star, a white dwarf, a G-type star, and verified with a globular cluster (see Boyer et al. 2022). Our own calculations of those offsets based on photometry for galaxies in our CEERS imaging data reduced with pmap-0956 (directly comparable with pmap-0959) are shown with smaller red circles, presenting an overall good agreement with the official recalibration released in pmap-0989. A re-evaluation of the zeropoint detector-to-detector offsets for the DR0.5 images released through this paper (calibrated with pmap-0989), is shown with larger blue circles, indicating residual offsets at the 2-4% level.

We used the CANDELS photometric catalog (Stefanon et al. 2017) to obtain synthetic magnitudes in the NIRCcam bands by convolving the filter transmission curves with the stellar population synthesis models best-fitting the spectral energy distributions of bright ($F160W < 24$ mag) galaxies. We then compared to Kron (1980) aperture photometry in the NIRCcam images. We confirmed the robustness of this method by using it on the four filters for which we had imaging data in similar filters, described in the previous paragraph. We obtained consistent results, compatible within 1-2%, but with a $1.5\times$ larger scatter.

Figure 11 shows our results comparing the detector-to-detector photometric calibration for pmap 0956 (before the recalibration released in pmap 0989, which we use in

this paper), compared with the recalibration work carried out with observations of three standard stars (PIDs 1536, 1537, and 1538), verified with data for a globular cluster (PID 1334) as described in Boyer et al. (2022), and used in a new NIRCcam zeropoints release in pmap 0989. We calculate the relative offsets of all SW detectors to B1. We apply a similar procedure to the F356W and F444W images, comparing them with IRAC $3.6\mu\text{m}$ and $4.5\mu\text{m}$ observations, respectively. We then calculate the relative offsets for these LW filters with respect to the BLONG detector. Our detector-to-detector relative calibrations based on galaxy photometry match (well within 2% in most cases) the results obtained with stars (which are better suited for flux calibration).

The two methods were also applied to the final mosaics described in this paper, in order to identify possible residual offsets in the relative calibration of the different detectors that might still be present in pmap 0989. The results are also shown in Figure 11. We detect offsets between detectors at the $< 5\%$ level, with a median of 2.5%. We do not apply these small offsets to our images at this time, but warn the reader that the relative and absolute calibration of NIRCcam images is still uncertain at the $\sim 5\%$ level.

Finkelstein et al. (2022, in prep) have also explored the accuracy of the photometric calibration by exploring what average offsets in flux calibration would be needed to minimize the colors between observations and best-fitting spectral templates for a sample of several hundred spectroscopically confirmed galaxies. They also find that the calibration is good to 1-2% in most bands, and no worse than $\sim 5\%$ (in the bluest bands). Again we note that these corrections were derived based on galaxies, and thus depend on aperture corrections. Future photometric calibration updates based on stellar observations will reduce the amplitude of these corrections.

4. KNOWN ISSUES

This first public data release of CEERS NIRCcam imaging represents a best-effort reduction given the version of the JWST pipeline and calibration reference files available at the time. Several aspects of our reduction will be improved in future versions. We briefly summarize the known issues regarding this current version.

First, the set of calibration reference files (pmap 0989) still includes some that were created pre-flight. As discussed in Section 3.2 and 3.3.5, the flats and flux calibration reference files are still preliminary. The current NIRCcam flats are ground flats that have been corrected to account for illumination variations present in early observations. According to the CRDS database (see footnote 1), the large-scale variations in the flat fields have been corrected to $\sim 1 - 2\%$, and ongoing programs to monitor sky flats and measure illumination patterns will continue to improve the flats. The photometric calibration reference files are the result of significant early efforts by the GTO and calibration teams, yet are still based on only a handful of observations. In Section 3.3.5, the photometric residuals from detector-to-detector are at the $\sim 2-5\%$ level. The relative and absolute calibrations will continue to improve with more observations and monitoring of photometric standards observed on each of the ten NIRCcam detectors. These programs (e.g., PIDs 1475, 1476, PI Boyer) and others will deliver iterative improvements to the reference files throughout Cycle 1.

Second, as mentioned in Section 3.1.2, the templates used for wisp subtraction include some source ghosts. At the time of their creation, there were not enough observations with sufficient dithers to successfully remove all input sources from a combined stack. As a result, some small regions are oversubtracted (at the $\sim 3 - 4\%$ level) in the CEERS images when we subtract the scaled templates. The wisp templates will continue to improve as more programs obtain NIRCcam imaging, allowing for cleaner stacks that capture the wisp patterns without contributions from sources. In the meantime, our background subtraction (Section 3.3.3) does an excellent job of removing any residual wisps or other background variations that may be introduced by our wisp subtraction.

Third, we note that the NIRCcam3 and NIRCcam6 mosaics exhibit more cosmic rays than the NIRCcam1 and NIRCcam2 images. This situation is expected given that the exposures in pointings 3 and 6 (a single dithered set of exposures per filter) are approximately two times longer than those in pointings 1 and 2 (where the depth is achieved in multiple sets of dithered exposures). In this reduction version, we have used the same reduction parameters for all four NIRCcam pointings. In the future, we will tune the jump detection step of Stage 1 and the outlier detection step of Stage 3 to ensure that cosmic rays and outliers are appropriately identified and flagged in all exposures.

Fourth, we have not yet performed a careful check for persistence in the majority of the NIRCcam images. We have masked out the very strong persistence in the additional F200W imaging in NIRCcam2 (Section 3.1.4), and that correction itself was an initial attempt that can be improved. In a future version we plan to stack each dither in pixel space (i.e., not aligned in WCS space) and identify sources that do not move on the detector from exposure to exposure and also perhaps fade with time. However, this method will not be able to identify persistence affecting extended sources that are larger than the dither size. We expect this approach to work well in NIRCcam1 and NIRCcam2, which have a minimum of six exposures in most filters, but three exposures per filter should be sufficient to identify compact cases persistence that can masquerade as high redshift galaxies.

Fifth, in creating the resampled mosaics, we do not make any correction for correlated noise. As discussed in Section 3.3.2 and Appendix D.4, we use `pixfrac` = 1 so that each output pixel is sufficiently covered by input pixels in pointings where there are only three dithers. However, drizzling the full input pixels (i.e., without “shrinking” the pixels first) results in a mosaic with correlated pixels. In this case, the noise in the resampled science images and variance maps is reduced by the cor-

relations, and so photometric uncertainties will be underestimated (e.g., Casertano et al. 2000; Labbé et al. 2003; Blanc et al. 2008; Whitaker et al. 2011; Papovich et al. 2016). We have rescaled the readnoise variance map to account for the sky variance (Section 3.3.2), but we have not yet applied any scaling to account for the pixel-to-pixel correlation introduced by the drizzling. This scaling can be estimated by computing the autocorrelation function of background, non-source pixels and determining the amount to which the noise has been suppressed (e.g., Guo et al. 2013).

Finally, we note that the F115W images are shallower than expected compared with the pre-launch exposure time calculator. As the background at these wavelengths is low, the images are dominated by readnoise to a larger degree than expected. Updates to the reference files related to detector noise properties as well as to processing methods may improve the depth in F115W slightly. However, we expect that the CEERS F115W images will remain ~ 0.2 - 0.3 magnitudes shallower than expected.

5. SUMMARY

We announce the public release of CEERS NIRCcam mosaics covering four pointings in the EGS field. These images were observed in June, 2022, and obtained in parallel to primary MIRI imaging. The NIRCcam imaging includes seven filters per pointing (F115W, F150W, F200W, F277W, F356W, F410M and F444W), reaching 5σ depths of $\sim 28.5 - 29.2$ for point sources.

We have reduced the images using version 1.7.2 of the *JWST* Calibration Pipeline, with additional steps and modifications developed to handle challenges encountered with the data. In Section 3, we describe our image reduction process in detail, including our custom corrections for snowballs, wisps, $1/f$ noise, astrometric alignment, variance map scaling, and background subtraction. We produce mosaics in each filter and field, resampled onto a common output grid with a pixel scale of $0''.03/\text{pixel}$ and aligned with available *HST* imaging in the field. Our reduction scripts and pipeline parameter files are summarized in Table 2 and will be available and documented on GitHub. The images are the result of a best-effort reduction with the available *JWST* pipeline and calibration reference files early in Cycle 1. In Section 4, we summarize issues with the current reduction version that will improve with updated information about instrument performance.

Our publicly released mosaics are available at ceers.github.io/dr05.html and on MAST via [10.17909/z7p0-8481](https://mast.stsci.edu/portal/#/search/ui/search/?query=10.17909/z7p0-8481). In the Appendix, we describe the file structure of the released images. We also describe previous CEERS

NIRCcam reductions that were used for results in some early CEERS publications.

Our reduction process has been heavily influenced by our work with our pre-flight NIRCcam simulations. We describe the creation of these simulations in Appendix C, using as input a mock galaxy catalog constructed with the Santa Cruz semi-analytic model, point sources and real $z \sim 9$ candidate galaxies. We describe the simulated image reduction in Appendix D, including a test of drizzle parameters that informed our parameter choices with the real images. Our NIRCcam simulations are available for download at ceers.github.io/sdr3.html.

1 We acknowledge that the location where this work took
 2 place, the University of Texas at Austin, that sits on in-
 3 digenous land. The Tonkawa lived in central Texas and
 4 the Comanche and Apache moved through this area. We
 5 pay our respects to all the American Indian and Indige-
 6 nous Peoples and communities who have been or have
 7 become a part of these lands and territories in Texas, on
 8 this piece of Turtle Island.

9 We thank Nikko Cleri, Rosemary Coogan, Asantha
 10 Cooray, Carlos Gómez-Guijarro, Nimish Hathi, Benne
 11 Holwerda and Marc Huertas-Company for a careful read
 12 of the manuscript. We thank the entire *JWST* team, in-
 13 cluding the engineers for making possible this wonder-
 14 ful over-performing telescope, the commissioning team
 15 for obtaining these early data, and the pipeline teams
 16 for their work over the years building and supporting
 17 the pipeline. The authors acknowledge the Texas Ad-
 18 vanced Computing Center (TACC) at The University
 19 of Texas at Austin for providing HPC and visualiza-
 20 tion resources that have contributed to the research re-
 21 sults reported within this paper. This work is based
 22 on observations with the NASA/ESA/CSA James Webb
 23 Space Telescope obtained from the Mikulski Archive for
 24 Space Telescopes at the Space Telescope Science Insti-
 25 tute (STScI), which is operated by the Association of
 26 Universities for Research in Astronomy (AURA), In-
 27 corporated, under NASA contract NAS5-03127. We
 28 acknowledge support from NASA through STScI ERS
 29 award JWST-ERS-1345. We thank Zolt Levay for mak-
 30 ing the beautiful color images of the CEERS NIRCcam
 31 and MIRI observations.

32 In this paper we refer to the *James Webb Space Tele-*
 33 *scope* using only the acronym *JWST*, reflecting our
 34 choice to celebrate the promise of this telescope without
 35 acknowledging the public official for whom it is named.
 36 This individual has been implicated in anti-LGBTQI+
 37 attitudes that do not reflect the authors' values related
 38 to inclusion in science.

Facilities: *JWST* (NIRCam), *HST* (ACS, WFC3), *Spitzer* (IRAC)

Software: Astropy (Astropy Collaboration et al. 2013), Besançon Model of the Galaxy (doi:10.25666/osu-theta.20210107.galaxy-model), Drizzle (Fruchter & Hook 2002), EAZY (Brammer et al. 2008), MIRAGE

(mirage-data-simulator.readthedocs.io), PHOTUTILS (Bradley et al. 2020), SciPy (Virtanen et al. 2020), SOURCE EXTRACTOR (Bertin & Arnouts 1996), STScI *JWST* Calibration Pipeline (jwst-pipeline.readthedocs.io)

APPENDIX

A. MOSAIC IMAGE STRUCTURE

We have produced a multi-extension fits file for each of the seven NIRCam filters for CEERS NIRCam pointings 1, 2, 3 and 6. These files are the result of all reduction steps described in Section 3. The files are available and documented at ceers.github.io/dr05.html and at MAST via [10.17909/z7p0-8481](https://archive.stsci.edu/missions/jwst/10.17909/z7p0-8481). The mosaics have 12 extensions, which we briefly summarize here:

- **SCI_BKSUB:** resampled, **background-subtracted** science data, in units of MJy/sr
- **SCI:** resampled science data (not background subtracted), in units of MJy/sr
- **ERR:** resampled uncertainty estimates as standard deviation, constructed as the sum in quadrature of the resampled variance maps
- **CON:** context image, which encodes information about the input images that contribute to each output pixel
- **WHT:** weight image giving the relative weight of the output pixels, constructed from the **VAR_RNOISE** array during resampling
- **VAR_POISSON:** resampled Poisson variance map
- **VAR_RNOISE:** resampled read noise variance map, which has been rescaled to include a robust estimate of the sky variance
- **VAR_FLAT:** resampled flat-field variance
- **BKGD:** the background model that was subtracted from the science image
- **BKGMASK:** the tiered source mask used to create the background
- **HDRTAB:** a table of FITS keyword values for all of the input images that were combined to produce the output image
- **ASDF:** metadata for the JWST data model

The extension **BKGD** can be computed by subtracting the **SCI_BKSUB** extension from the **SCI** extension, but we include it in the mosaics for completeness.

We also provide images in six *HST* ACS and WFC3 filters, cut out from the full EGS mosaics and pixel-aligned to each CEERS NIRCam pointing. While the background in the *HST* filters was already very close to zero, we have background-subtracted these mosaics for consistency with the NIRCam images and provide the *HST* mosaics both with and without this subtraction. The *HST* mosaics have five extensions, which we summarize here:

- **SCI_BKSUB:** resampled, **background-subtracted** science data, in units of counts/s
- **SCI:** resampled science data (not background subtracted), in units of counts/s
- **rms:** resampled uncertainty estimates as standard deviation
- **BKGD:** the background model that was subtracted from the science image
- **BKGMASK:** the tiered source mask used to create the background

B. EARLIER CEERS DATA REDUCTIONS

Here we briefly describe the previous versions of the CEERS NIRCam data reduction that were used for results presented in early papers from the CEERS team.

B.1. Version 0.05, Zavala et al. (2022)

Zavala et al. (2022) presented results based on version 0.05 of the CEERS NIRCam reduction, which used JWST version 1.5.3 and pmap 0932 (NIRCam imap 0214). This reduction involved a preliminary correction for $1/f$ noise, but did not correct for snowballs or wisps. The astrometric alignment for this version should also be considered preliminary. We calculated astrometric corrections for groups of images, rather than individually for each detector and dither. Specifically, we fit module A and B separately for the LW images (grouping all dithers

for a given filter and module together), and fit the SW images in three sets: (1) all module A detectors, (2) detector B2, which demonstrated significant offsets from the other B detectors, and (3) the remaining three detectors of Module B. We first aligned the F200W images to the *HST*/WFC3 F160W reference catalog tied to Gaia-EDR3, and then used `PHOTUTILS` to create a new reference catalog in F200W. We cleaned the F200W reference catalog of all sources near detector edges and spurious sources around diffraction spikes and in the noise around bright sources, and considered only compact sources in the magnitude range $18 < m_{200} < 27$. We aligned each NIRCcam filter to F200w using the three groups mentioned above. The median astrometric offset in each filter and NIRCcam pointing is $\lesssim 0''.005$, and the RMS is $\sim 0''.025\text{--}0''.03$ (~ 1 pixel). However, for NIRCcam pointing 2 in particular, the astrometry in the F115W and F150W filter suffered from a larger global offset of $\sim 2\text{--}3$ pixels. Additionally, the alignment between the images in each dither for this pointing was off by ~ 0.5 pixels, which slightly smeared out a small percentage of source flux, especially problematic for compact sources.

B.2. Version 0.07, *Finkelstein et al. (2022b)*, *Guo et al. (2022)* and *Kocevski et al. (2022)*

Finkelstein et al. (2022b), *Guo et al. (2022)* and *Kocevski et al. (2022)* presented results based on version 0.07 of the CEERS NIRCcam reduction, which used `JWST` version 1.6.2 and `pmap` 0942 (NIRCcam `imap` 0221). This reduction version included `wisp` subtraction and an improved $1/f$ noise removal. It did not include a correction for snowballs, though we note that the authors of each paper carefully inspected individual exposures to ensure their results were not affected by snowballs. This reduction version also implemented the local background subtraction on the mosaics that is described in Section 3.3.3.

Finkelstein et al. (2022b) presented an earlier arXiv version that used version 0.05 (see previous section), where the improved astrometric alignment had a significant effect on their results. The measured F150W flux of the high-redshift candidate Maisie’s Galaxy increased sufficiently in v0.07 to change the best-fit photometric redshift from $z \sim 14$ to a more tightly-constrained $z \sim 12$. The authors have provided a full description of how the reduction version changed their results.⁷

C. SIMULATED CEERS NIRCAM IMAGING

In preparation for CEERS *JWST*/NIRCcam imaging data, we created a series of simulated NIRCcam images designed to reproduce the CEERS observing strategy.

These simulations were designed to aid in our preparations with reducing the real imaging as well as to validate our photometry and analysis methods for the real NIRCcam imaging. The simulations are performed with the Multi-Instrument Ramp Generator⁸ (`MIRAGE`), with input sources taken from a mock catalog created using the Santa Cruz semi-analytic model for galaxy formation. In the following sections, we describe the simulation inputs and creation.

C.1. Santa Cruz SAM Mock Galaxy Catalog

The mock images are simulated based on an augmented version⁹ of the mock galaxy catalog presented in *Yung et al. (2022)*. The simulated lightcone spans 782 arcmin² with coordinates overlapping with the observed EGS field and containing galaxies over redshift range $0 < z \lesssim 10$ and rest-frame M_{UV} range $-16 \gtrsim M_{UV} \gtrsim -22$. The galaxies in the mock lightcone are simulated with the Santa Cruz semi-analytic model (SAM) for galaxy formation (*Somerville et al. 2015, 2021*). Within dark matter halos extracted from the Bolshoi-Planck simulation (*Klypin et al. 2016*) and Monte Carlo merger trees generated with the extended Press-Schechter formalism (e.g. *Somerville & Kolatt 1999*), the SAM tracks the evolution of global galaxy properties under the influence of a set of carefully curated physical processes, including cosmological accretion, cooling, star formation, chemical enrichment, and stellar and AGN feedback. We refer the reader to *Yung et al. (2022)* for a schematic flowchart that illustrates the internal workflow of the SAM. The model configuration and physical parameters are based on the calibration from *Yung et al. (2019a)* and *Yung et al. (2021)*. The models have been shown to reproduce the observed evolution in high-redshift (e.g. $z \gtrsim 4$) one-point distribution functions of M_{UV} , M_* , and SFR (*Yung et al. 2019a,b*), observational constraints on the IGM reionization history (*Yung et al. 2020b,a*), as well as two-point auto-correlation functions from $0 \lesssim z \lesssim 7.5$ (*Yung et al. 2022*).

The full star formation and chemical enrichment histories of individual predicted galaxies are forward modelled into rest- and observed-frame photometry with SEDs generated based on stellar the population synthesis (SPS) models of *Bruzual & Charlot (2003)*. The observed-frame photometry is calculated accounting for dust attenuation effects using the attenuation curve of *Calzetti et al. (2000)*, and for absorption by hydrogen along the line of sight in the IGM (*Madau et al. 1996*). In the CEERS mock catalogs, we also include

⁷ web.corral.tacc.utexas.edu/ceersdata/papers/Maisie_update.pdf

⁸ mirage-data-simulator.readthedocs.io

⁹ <https://ceers.github.io/sdr3.html#catalogs>, SDR V3

self-consistently predicted nebular emission lines excited by young stars, AGN, and post-AGB stellar populations in the high-resolution synthetic spectra and the broad- and medium-band photometry (Hirschmann et al. 2017, Hirschmann et al. 2019; Yung, Hirschmann, Somerville et al., in prep.) Galaxies are added to the images as Sérsic profiles (Sérsic 1963, 1968), with Sérsic indices and effective radii determined as described in Brennan et al. (2015).

C.2. Additional Simulation Inputs

In addition to the mock galaxy catalog, we have added two additional sets of sources to the CEERS simulations. First, we have included the seven $z \sim 9$ galaxy candidates in the EGS field presented by Finkelstein et al. (2022a). This sample represents a significant (2σ) overdensity in the EGS field (Finkelstein et al. 2022a), including two spectroscopically-confirmed galaxies at $z = 8.683$ (Zitrin et al. 2015) and $z = 8.665$ (Larson et al. 2022). The seven galaxies are added as Sérsic profiles at their expected coordinates, and their *JWST* photometry is estimated using the best-fit EAZY template for each source’s *HST* and *Spitzer* photometry.

Second, we included point sources in the NIRCam imaging simulations in two ways. The positions and magnitudes of bright ($V < 16$, Vega magnitudes) point sources in the EGS field are added from 2MASS, *WISE* and *Gaia*. We added fainter point sources ($16 < V < 29$ Vega) using the Besançon Model¹⁰ at mock positions to approximate the expected stellar density and luminosity distribution in the EGS field. In both cases, **MIRAGE** adds point sources from a library of PSFs, which was constructed using **WebbPSF** (Perrin et al. 2014). We use the default PSF library included with the **MIRAGE** reference files. This gridded library includes an image of the PSF core and an additional image of the PSF wings for each filter and pupil combination at a grid of positions across each detector. For each source, the appropriate PSF is selected from this library, the core is combined with the image of the wings, and the full PSF is normalized and scaled to the required brightness. The separation of the core and wings allows the user to tune the size of the PSFs in the simulated images. In the interest of decreasing processing time for the CEERS simulations, we adopted the default size of the PSF wing images (301×301 pixels) at all magnitudes. As a result, we note that the PSFs of some sources in our simulated images appear truncated. We found this an acceptable compromise as our science goals for the simulations were

focused on the identification and recovery of galaxy colors at high redshift.

C.3. Simulating Raw Images with **MIRAGE**

With these inputs, we use **MIRAGE** to construct raw NIRCcam exposures that approximate the CEERS observations and include realistic estimates of noise, sky background level, and detector artifacts. The Astronomer’s Proposal Tool (APT) file defines the observation specifications, setting the filters, readout modes and patterns, and dithers. At the time of our simulation creation, **MIRAGE** could not parse an observing setup with either MIRI or NIRSpec as the primary instrument and NIRCcam imaging in parallel. However, as the parallel dithers are specified according to the primary observation (determined by either the size of the MIRI PSF or the NIRSpec nodding pattern), the combined primary+NIRCcam parallel specifications were crucial. We therefore created a separate, NIRCcam-only APT file with the same targets, number of dithers, and the same exposure specifications as the real CEERS program. We then replaced the pointing information of this NIRCcam-only mock program with that from the original CEERS APT file. In this way, we were able to create a set of parameter files as input to **MIRAGE** that replicated all of the CEERS dither patterns. We note that this approach is no longer required, as **MIRAGE** can parse all observation templates and primary-parallel combinations.

The full CEERS NIRCcam imaging simulation involves creating 1816 separate images, one image per exposure for each of the ten NIRCcam detectors. This total includes 75 exposures obtained in parallel to NIRSpec MSA observations, 57 exposures in parallel to MIRI imaging, and 56 exposures taken with the NIRCcam WFSS observing mode. For these simulations we include just the imaging portion of the NIRCcam WFSS observations, which amounts to a total of 24 direct image exposures in F356W and 56 SW exposures in F115W. We separately produced simulated CEERS NIRCcam WFSS observations, which are available for download at ceers.github.io/sdr3.html.

For each simulated image, **MIRAGE** works in three stages. It first creates a noiseless seed image of the input point sources and galaxies as well as any requested background signals. We adopted the beginning of the CEERS June observing window (15-17 June, 2022) as simulated observing date, and **MIRAGE** used the **jwtst.backgrounds**¹¹ tool to estimate the appropriate value for the EGS field on this date. In the second

¹⁰ doi:10.25666/osu-theta.20210107.galaxy-model

¹¹ github.com/spacetelescope/jwst_backgrounds

stage, **MIRAGE** reconstructs a dark exposure to match the required readout pattern with the specified number of groups and integrations. The use of ground-tested dark exposures introduces real detector effects such as the bias, known hot pixels, and detector noise properties. Finally, **MIRAGE** combines the dark with the seed image and adds additional effects such as cosmic rays. We used **MIRAGE** version 2.2.1 and the CRDS pmap 0834 (NIRCam instrument map 0193) for the input reference files.

D. REDUCING RAW SIMULATED DATA

While we leave the bulk of our discussion of our data reduction to Section 3, here we summarize our steps processing the raw simulated data. We do this for two reasons: (1) these processing steps informed our methods for working with the real CEERS NIRCam imaging, and (2) we aim to provide a reference for how the simulated products were processed for any who wish to use them for science.

We process the raw simulated images through the three stages of the **JWST** pipeline, with custom scripts we developed to handle differences between the **JWST** reference files available at the time of simulation and the input assumptions of **MIRAGE**. The reduction uses **JWST** version 1.4.6 except where noted, and CRDS pmap 0834 for consistency with the simulated inputs. We adopt most of the default parameters for the **JWST** steps and describe any changes below. For the detector-level corrections applied in Stage 1, we apply the correction for interpixel capacitance, skipped by default, because **MIRAGE** adds this effect to the simulated data. We also supply custom gain maps for the steps that identify jumps in the up-the-ramp signal and fit the ramp to obtain a countrate map. These custom gain maps were created to match the average value per detector that **MIRAGE** uses in creating the images, rather than the location-varying gain maps that were present in the reference files at the time.

Our first custom step is to remove the $1/f$ noise that is present in the images as horizontal and vertical striping. In short, this correction involves masking out all bad pixels and source flux (using the seed images for source positions and footprints) and collapsing each image along columns and rows to measure the striping pattern. We developed this correction in working with this simulated data, and improved on the process for the real images. We describe this step in detail in Section 3.1.3.

D.1. Custom Flat Fields

Following the calibration steps of Stage 2, we perform a correction to remove residual large-scale but low-level

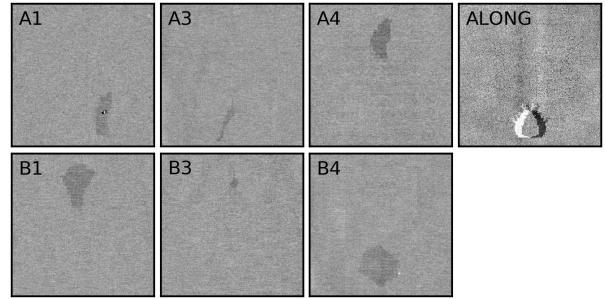


Figure 12. Custom flat field images we created for the reduction of our simulated images. We show the SW detectors A1, A3, A4, B1, B3, B4, each of which has a different low-level feature present, caused by areas on the detectors with thinner epoxy layers. We use these six custom flats in reducing our simulated images. We also show an earlier custom flat we created for the LW detector ALONG. This feature was present in our SDR1 images and is included here for reference. With updated **MIRAGE**, **JWST**, and CRDS reference file versions, we no longer see this ALONG feature in our simulated images.

features present in some of the images. The features correspond to areas on the detectors where the epoxy layer is thinner than for the unaffected pixels.¹² We found that these epoxy voids are multiplicative features in our simulated images and can be removed in a similar fashion as applying a flat field. The affected detectors are SW A1, A3, A4, B1, B3 and B4. In a previous version of our simulations (created using **MIRAGE** version 2.1.0, **JWST** version 1.3.3 and pmap 0764), we found a prominent feature only on detector A5 that is not present in our new CEERS simulations. We believe the changing nature of these epoxy voids in our simulations may be caused by updates in the reference files used to add detector features to the images, such that the presence and strength of the features is determined by a combination of CRDS context and **MIRAGE** and **JWST** versions.

We therefore created custom flat fields for the six affected SW detectors in the following way. For each detector and filter we created 33 blank simulated images (chosen because each affected filter has at least 33 exposures across the full CEERS field) with no input sources and no cosmic rays added. We used the same input parameter files as used for the simulated images to ensure that the exact observation specifications were replicated. However, we changed the Poisson seeds so that the noise added to the blank images was pulled from a unique distribution. We processed the blank images following the same **JWST** and custom steps as the images contain-

¹² e.g., STScI Technical Document **JWST-STScI-004622**, Hilbert & Rest, 2014.

ing sources. For the $1/f$ noise removal, we masked out the features so they would not contribute to the measurement of the striping patterns. After flat-fielding the blank images, we normalized each image by its median and combined all 33 using a weighted mean. The weights were taken as $w_i = 1/ERR_i^2$, the uncertainty of the output flat field was estimated as $\sqrt{1/\sum w_i}$, and both the combined data and error arrays were normalized by the output image median. Figure 12 shows the six custom flats we created for the SW detectors. We also show a custom flat for LW detector ALONG that we created for a previous version of our simulated images (SDR1). This ALONG feature is not present in our current simulations and is included here for reference. We apply these six custom flats to the relevant detector images after the real flat is applied but before the flux calibration step that converts the images to MJy/sr.

D.2. Sky Subtraction

The final stage of JWST includes a step (`SkyMatch`) that computes sky values in a collection of images in a way that matches the sky levels of several images before they are combined to form a mosaic. However, we found that the `SkyMatch` step does not properly remove the background in simulated CEERS images when run on a collection of images. This is likely due to a mismatch between the input photometric calibration parameters used by `MIRAGE` in simulating the data and those used by JWST. Specifically, `MIRAGE` translates input magnitudes into count rates using *HST*-style `PHOTFLAM` values derived from filter throughput curves. `MIRAGE` uses the same `PHOTFLAM` value for all short wavelength detectors for a given module and filter. The pipeline, however, converts count rates to MJy/sr using the `PHOTMJYSR` parameter in the flux calibration reference file, which depends on the pixel area and a mean gain value, both of which vary from detector to detector. A single value does not exist that can bring all simulated detector images to the same background level. Additionally, the CEERS dithers are not large enough to cover the gaps between detectors, and so there are many exposures with no overlap area in common for globally matching the sky values.

We find that the background levels in the final mosaics are significantly improved if `SkyMatch` is run on each calibrated image individually before mosaic creation. For this step, we adopt some minor changes to the default parameter values used to calculate the sky statistics. We tested a grid of these parameter values and find that the following parameters yield output images with median backgrounds closest to zero for the CEERS simulated data. We set the upper and lower sigma clipping limits

to 2σ (from the default of 4σ), the upper limit of usable pixel values for sky computation to 1 MJy/sr, and the number of clipping iterations to 10 (default=5).

D.3. Astrometry and Outlier Rejection

Before creating mosaics, Stage 3 of JWST includes processing steps to apply astrometric corrections and identify outliers in the images. In real data, astrometric alignment is needed to account for uncertainties in guide star positions and correct any remaining distortions or offsets between images from different detectors. However, as the simulated images are not created with astrometric errors or offsets from exposure to exposure, there is no need to perform this correction.

Next, the `OutlierDetection` step of JWST Stage 3 builds a stack of input images resampled onto a common grid in order to identify bad pixels or cosmic rays that were not detected in the `Jump` step of Stage 1. We found that a bug in the JWST version 1.4.6 pipeline sometimes calculated incorrect WCS bounding boxes for the stacks. Occasionally, the bounding box would exclude a portion of some input images, resulting in all source flux from the region being flagged as outliers. Therefore, we use JWST version 1.5.2 for the `OutlierDetection` step. Once outlier pixels are identified and flagged, we return to using version 1.4.6 for mosaicking for consistency with the rest of the reduction.

D.4. Simulated Mosaic Creation

Images are coadded in the Stage 3 step `Resample` as described in Section 3.3.2, with an output pixel scale of $0''.03/\text{pix}$ and `pixfrac`=1. We chose these drizzle parameters based on tests that we describe in the next paragraph, performed with simulated images of point sources. The mosaics are all drizzled onto a common WCS such that they are pixel-aligned across all filters, though they are not aligned with the *HST* mosaics as the mock NIRCcam sources do not have counterparts in the *HST* images. We note that due to pixels with a value of exactly zero in the variance arrays of input images, there are “holes” present in the error arrays of our simulated mosaics as described in Section 3.3.2.

In order to determine the optimal output pixel scale and `pixfrac`, we created a simulated NIRCcam pointing containing point sources and tested the FWHM recovery for different output pixel scales and `pixfrac` values. We placed 72 point sources across the image, with a magnitude $m = 23$ in all filters to avoid saturating the detectors in a CEERS-length exposure. This PSF simulation uses the observation specification of a NIRCcam imaging pointing obtained in parallel to the NIRCspec MSA primary observations, and so uses three small

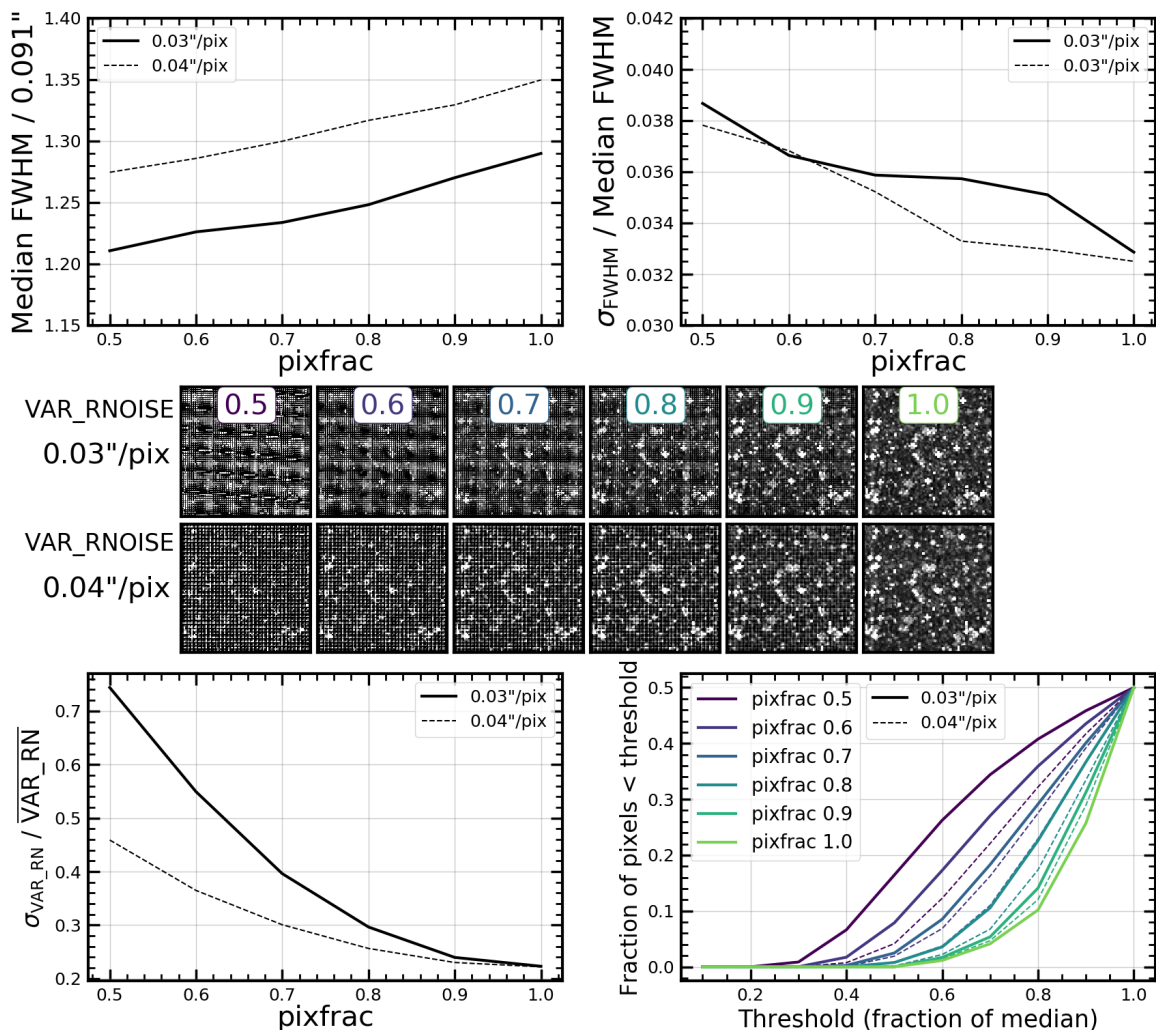


Figure 13. Example of the drizzle tests we performed with simulated images containing 72 point sources and varying the output pixel scales and `pixfrac` values. The plots here show results for F277W, for which we explored $0''.03/\text{pixel}$ and $0''.04/\text{pixel}$ output pixel scales. In the top row we show the median recovered FWHM normalized by intrinsic FWHM (left) and the standard deviation of the 72 recovered FWHMs normalized by the median (right), both as a function of `pixfrac`. In the middle panels, we show small regions of the `VAR_RNOISE` arrays for each pixel scale and `pixfrac`, all plotted with the same image stretch and scale. These panels illustrate the decreasing readnoise with increasing pixel scale and/or `pixfrac`. In the bottom left panel we show the normalized standard deviation of sigma-clipped pixel values in the `VAR_RNOISE` as a function of `pixfrac`. In the bottom right panel we plot the fraction of pixels in the inverse `VAR_RNOISE` arrays that lie below various thresholds as an way to quantify the number of outlier pixels in each mosaic. These tests informed our choice to adopt an output pixel scale of $0''.03/\text{pixel}$ and a `pixfrac` of 1 for the mosaics in our first data release.

dithers determined by the NIRSpec nods. We explored output pixel scales of $0''.015/\text{pixel}$ and $0''.02/\text{pixel}$ in the SW images and $0''.03/\text{pixel}$ and $0''.04/\text{pixel}$ in the LW images. These choices are motivated by the need for the pixel scales of the SW and LW images to be integer multiples of each other (and all NIRCam images to be integer multiples of the available *HST* imaging) to maintain alignment. We tested `pixfrac` values ranging from 0.5 to 1.

In Figure 13, we show a summary of the results of these tests for F277W as an example (comparing mosaics with $0''.03/\text{pixel}$ and $0''.04/\text{pixel}$). First, we

measured the recovered FWHM of all 72 point sources. In the top left panel, we show the median recovered FWHM as a function of `pixfrac` normalized by the reported FWHM for this filter¹³ ($0.091''$). The median of the recovered FWHMs increases towards larger `pixfracs`, which is expected due to the increased pixel-

¹³ The documented FWHMs are based on oversampled simulated PSFs created with WebbPSF. The PSFs will be updated during Cycle 1 based on in-flight measurements. See jwst-docs.stsci.edu/jwst-near-infrared-camera/nircam-performance/nircam-point-spread-function

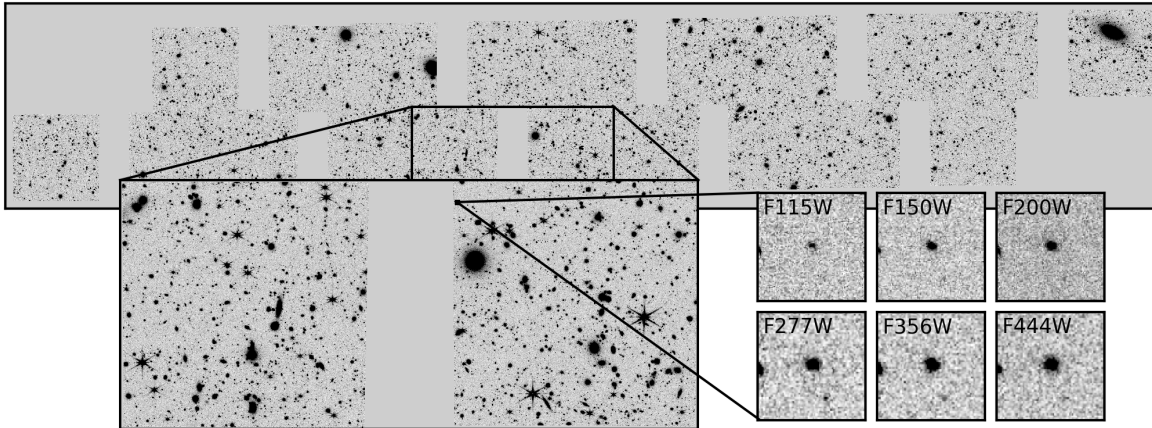


Figure 14. The full CEERS simulated field, including all ten NIRCcam pointings. Here we show the F277W mosaic and a zoom-in around pointing 5, which was the focus of our early simulated data release. We further zoom in around one of the real $z \sim 9$ candidate galaxies that has been added to this field (see Section C.2). We show $3''$ postage stamps of the simulated images of this galaxy in all filters.

to-pixel correlations in the drizzled images. The recovered FWHMs are $\sim 5\%$ larger for the $0''.04/\text{pixel}$ scale, indicating a preference for the smaller pixel scale. We also calculated the standard deviation of the recovered FWHMs, and plot these values normalized by the median recovered FWHM in the top right panel. For both pixel scales, the normalized σ_{FWHM} decreases with increasing `pixfrac`, an expected trend as the output pixels more fully sample the PSFs.

Next we measured the noise properties in the drizzled mosaics. In the bottom left panel of Figure 13, we plot the standard deviation of the sigma-clipped pixel values in the `VAR.RNOISE` maps normalized by the mean. These curves fall with increasing `pixfrac`, indicating that the width of the noise distribution decreases as more of each input pixel is incorporated into the output pixels. We also measured the fraction of pixels in the inverse variance maps ($1/\text{VAR.RNOISE}$) that are a certain distance away from the median. In this way, we can quantify the number and magnitude of outlier pixels as a function of `pixfrac`. These curves are shown in the lower right panel of Figure 13, color-coded by `pixfrac`. We once again see that the fraction of outliers decreases with increasing `pixfrac`. In the center of Figure 13, we show a small region of the `VAR.RNOISE` maps for each output pixel scale and `pixfrac`. These postage stamps are all displayed with the same scale and stretch and provide a visual representation of how well the output pixels are sampled in each mosaic. The readnoise is reduced in mosaics with the larger pixel scale and/or larger `pixfrac`.

These tests informed our decision to create mosaics on output pixel scales of $0''.03/\text{pixel}$ and `pixfrac`=1. This choice of `pixfrac` does result in maximum correlated noise introduced during the drizzle process, which we discuss in Section 4. We note that a `pixfrac` of 0.9 or

0.8 may also be acceptable, and we will explore these options more completely in a future reduction. We plan to use these mosaics (both for the simulated and real NIRCcam data) for source detection and photometry in all filters. For future data releases, we will create SW mosaics on an output scale of $0''.015/\text{pixel}$ for use characterizing source morphologies.

Finally, we note that the mosaic creation for the full CEERS simulated mosaic (all ten NIRCcam pointings) requires a considerable amount of memory. This version of the pipeline holds all images, variance maps, and weight maps in memory while resampling each onto the common output grid. With 928 input images, the F115W mosaic is especially memory intensive, requiring almost one terabyte of memory to resample all input images onto a $0''.03/\text{pixel}$ output image (and an estimated 3.5 TB for an output $0''.015/\text{pixel}$ scale). We therefore use the Frontera computing system at TACC to create these mosaics.

D.5. Simulated Raw and Reduced Data Products

We have provided two sets of simulated NIRCcam images as part of public CEERS data releases. In CEERS Simulated Data Release 1 (SDR1¹⁴), we shared a preliminary set of simulations of a single CEERS NIRCcam pointing (labeled CEERS5), along with detailed step-by-step instructions for reducing the images in a Jupyter notebook. We also presented this work as part of JWWebinar 13. The mosaics released in SDR1 had pixel scales of $0''.015/\text{pixel}$ in the SW filters, and $0''.03/\text{pixel}$ in the LW filters. Next, we shared an updated simulation and reduction of this single NIRCcam pointing

¹⁴ ceers.github.io/sdr1.html

in CEERS Simulated Data Release 3 (SDR3¹⁵). This follow-up release incorporated improvements in our input mock galaxy catalog and **MIRAGE**, as well as updates to **JWST** and the reference files available at the time. These mosaics were all drizzled to an output pixel scale

of $0''.03/\text{pixel}$, and were pixel-aligned across all filters. In Figure 14, we show the full CEERS simulated mosaic, including a panel zooming in to pointing 5, the pointing shared in SDR1 and SDR3. We further zoom in on simulated imaging in all filters of one of the real $z \sim 9$ candidates.

REFERENCES

- Astropy Collaboration, Robitaille, T. P., Tollerud, E. J., et al. 2013, *A&A*, 558, A33, doi: [10.1051/0004-6361/201322068](https://doi.org/10.1051/0004-6361/201322068)
- Bagley, M. B., Finkelstein, S. L., Rojas-Ruiz, S., et al. 2022, arXiv e-prints, arXiv:2205.12980. <https://arxiv.org/abs/2205.12980>
- Beichman, C. A., Rieke, M., Eisenstein, D., et al. 2012, in Society of Photo-Optical Instrumentation Engineers (SPIE) Conference Series, Vol. 8442, Space Telescopes and Instrumentation 2012: Optical, Infrared, and Millimeter Wave, ed. M. C. Clampin, G. G. Fazio, H. A. MacEwen, & J. Oschmann, Jacobus M., 84422N, doi: [10.1117/12.925447](https://doi.org/10.1117/12.925447)
- Bertin, E., & Arnouts, S. 1996, *Astronomy and Astrophysics Supplement Series*, 117, 393, doi: [10.1051/aas:1996164](https://doi.org/10.1051/aas:1996164)
- Blanc, G. A., Lira, P., Barrientos, L. F., et al. 2008, *ApJ*, 681, 1099, doi: [10.1086/588018](https://doi.org/10.1086/588018)
- Boyer, M. L., Anderson, J., Gennaro, M., et al. 2022, *Research Notes of the American Astronomical Society*, 6, 191, doi: [10.3847/2515-5172/ac923a](https://doi.org/10.3847/2515-5172/ac923a)
- Bradley, L., Sipócz, B., Robitaille, T., et al. 2020, *astropy/photutils: 1.0.0*, Zenodo, Zenodo, doi: [10.5281/zenodo.4044744](https://doi.org/10.5281/zenodo.4044744)
- Brammer, G. B., van Dokkum, P. G., & Coppi, P. 2008, *ApJ*, 686, 1503, doi: [10.1086/591786](https://doi.org/10.1086/591786)
- Brennan, R., Pandya, V., Somerville, R. S., et al. 2015, *MNRAS*, 451, 2933, doi: [10.1093/mnras/stv1007](https://doi.org/10.1093/mnras/stv1007)
- Bruzual, G., & Charlot, S. 2003, *MNRAS*, 344, 1000, doi: [10.1046/j.1365-8711.2003.06897.x](https://doi.org/10.1046/j.1365-8711.2003.06897.x)
- Calzetti, D., Armus, L., Bohlin, R. C., et al. 2000, *ApJ*, 533, 682, doi: [10.1086/308692](https://doi.org/10.1086/308692)
- Casertano, S., de Mello, D., Dickinson, M., et al. 2000, *AJ*, 120, 2747, doi: [10.1086/316851](https://doi.org/10.1086/316851)
- Finkelstein, S. L., Bagley, M., Song, M., et al. 2022a, *ApJ*, 928, 52, doi: [10.3847/1538-4357/ac3aed](https://doi.org/10.3847/1538-4357/ac3aed)
- Finkelstein, S. L., Bagley, M. B., Arrabal Haro, P., et al. 2022b, arXiv e-prints, arXiv:2207.12474. <https://arxiv.org/abs/2207.12474>
- Fruchter, A. S., & Hook, R. N. 2002, *PASP*, 114, 144, doi: [10.1086/338393](https://doi.org/10.1086/338393)
- Gardner, J. P., Mather, J. C., Clampin, M., et al. 2006, *SSRv*, 123, 485, doi: [10.1007/s11214-006-8315-7](https://doi.org/10.1007/s11214-006-8315-7)
- Grogin, N. A., Kocevski, D. D., Faber, S. M., et al. 2011, *ApJS*, 197, 35, doi: [10.1088/0067-0049/197/2/35](https://doi.org/10.1088/0067-0049/197/2/35)
- Guo, Y., Ferguson, H. C., Giavalisco, M., et al. 2013, *ApJS*, 207, 24, doi: [10.1088/0067-0049/207/2/24](https://doi.org/10.1088/0067-0049/207/2/24)
- Guo, Y., Jogee, S., Finkelstein, S. L., et al. 2022, arXiv e-prints, arXiv:2210.08658. <https://arxiv.org/abs/2210.08658>
- Hirschmann, M., Charlot, S., Feltre, A., et al. 2017, *MNRAS*, 472, 2468, doi: [10.1093/MNRAS/STX2180](https://doi.org/10.1093/MNRAS/STX2180)
- . 2019, *MNRAS*, 487, 333, doi: [10.1093/mnras/stz1256](https://doi.org/10.1093/mnras/stz1256)
- Jakobsen, P., Ferruit, P., Alves de Oliveira, C., et al. 2022, *A&A*, 661, A80, doi: [10.1051/0004-6361/202142663](https://doi.org/10.1051/0004-6361/202142663)
- Klypin, A., Yepes, G., Gottlöber, S., Prada, F., & Heß, S. 2016, *MNRAS*, 457, 4340, doi: [10.1093/mnras/stw248](https://doi.org/10.1093/mnras/stw248)
- Kocevski, D. D., Barro, G., McGrath, E. J., et al. 2022, arXiv e-prints, arXiv:2208.14480. <https://arxiv.org/abs/2208.14480>
- Koekemoer, A. M., Faber, S. M., Ferguson, H. C., et al. 2011, *ApJS*, 197, 36, doi: [10.1088/0067-0049/197/2/36](https://doi.org/10.1088/0067-0049/197/2/36)
- Kriek, M., Shapley, A. E., Reddy, N. A., et al. 2015, *The Astrophysical Journal Supplement Series*, 218, 15, doi: [10.1088/0067-0049/218/2/15](https://doi.org/10.1088/0067-0049/218/2/15)
- Kron, R. G. 1980, *ApJS*, 43, 305, doi: [10.1086/190669](https://doi.org/10.1086/190669)
- Labbé, I., Franx, M., Rudnick, G., et al. 2003, *AJ*, 125, 1107, doi: [10.1086/346140](https://doi.org/10.1086/346140)
- Larson, R. L., Finkelstein, S. L., Hutchison, T. A., et al. 2022, arXiv e-prints, arXiv:2203.08461. <https://arxiv.org/abs/2203.08461>
- Madau, P., Ferguson, H. C., Dickinson, M. E., et al. 1996, *MNRAS*, 283, 1388, doi: [10.1093/mnras/283.4.1388](https://doi.org/10.1093/mnras/283.4.1388)
- Nardiello, D., Bedin, L. R., Burgasser, A., et al. 2022, *MNRAS*, 517, 484, doi: [10.1093/mnras/stac2659](https://doi.org/10.1093/mnras/stac2659)
- Newman, J. A., Cooper, M. C., Davis, M., et al. 2013, *ApJS*, 208, 5, doi: [10.1088/0067-0049/208/1/5](https://doi.org/10.1088/0067-0049/208/1/5)

¹⁵ ceers.github.io/sdr3.html

- Oke, J. B., & Gunn, J. E. 1983, *ApJ*, 266, 713, doi: [10.1086/160817](https://doi.org/10.1086/160817)
- Papovich, C., Shipley, H. V., Mehrrens, N., et al. 2016, *ApJS*, 224, 28, doi: [10.3847/0067-0049/224/2/28](https://doi.org/10.3847/0067-0049/224/2/28)
- Perrin, M. D., Sivaramakrishnan, A., Lajoie, C.-P., et al. 2014, in *Society of Photo-Optical Instrumentation Engineers (SPIE) Conference Series*, Vol. 9143, *Space Telescopes and Instrumentation 2014: Optical, Infrared, and Millimeter Wave*, ed. J. Oschmann, Jacobus M., M. Clampin, G. G. Fazio, & H. A. MacEwen, 91433X, doi: [10.1117/12.2056689](https://doi.org/10.1117/12.2056689)
- Rieke, G. H., Wright, G. S., Böker, T., et al. 2015, *PASP*, 127, 584, doi: [10.1086/682252](https://doi.org/10.1086/682252)
- Rieke, M. J., Kelly, D., & Horner, S. 2005, in *Society of Photo-Optical Instrumentation Engineers (SPIE) Conference Series*, Vol. 5904, *Cryogenic Optical Systems and Instruments XI*, ed. J. B. Heaney & L. G. Burriesci, 1–8, doi: [10.1117/12.615554](https://doi.org/10.1117/12.615554)
- Rieke, M. J., Baum, S. A., Beichman, C. A., et al. 2003, in *Society of Photo-Optical Instrumentation Engineers (SPIE) Conference Series*, Vol. 4850, *IR Space Telescopes and Instruments*, ed. J. C. Mather, 478–485, doi: [10.1117/12.489103](https://doi.org/10.1117/12.489103)
- Rigby, J., Perrin, M., McElwain, M., et al. 2022, arXiv e-prints, arXiv:2207.05632. <https://arxiv.org/abs/2207.05632>
- Schlawin, E., Leisenring, J., Misselt, K., et al. 2020, *AJ*, 160, 231, doi: [10.3847/1538-3881/abb811](https://doi.org/10.3847/1538-3881/abb811)
- Sérsic, J. L. 1963, *Boletín de la Asociación Argentina de Astronomía La Plata Argentina*, 6, 41
- . 1968, *Atlas de Galaxias Australes*
- Somerville, R. S., & Kolatt, T. S. 1999, *MNRAS*, 305, 1, doi: [10.1046/j.1365-8711.1999.02154.x](https://doi.org/10.1046/j.1365-8711.1999.02154.x)
- Somerville, R. S., Popping, G., & Trager, S. C. 2015, *MNRAS*, 453, 4337, doi: [10.1093/mnras/stv1877](https://doi.org/10.1093/mnras/stv1877)
- Somerville, R. S., Olsen, C., Yung, L. Y. A., et al. 2021, *MNRAS*, 502, 4858, doi: [10.1093/mnras/stab231](https://doi.org/10.1093/mnras/stab231)
- Stefanon, M., Yan, H., Mobasher, B., et al. 2017, *ApJS*, 229, 32, doi: [10.3847/1538-4365/aa66cb](https://doi.org/10.3847/1538-4365/aa66cb)
- Virtanen, P., Gommers, R., Oliphant, T. E., et al. 2020, *Nature Methods*, 17, 261, doi: [10.1038/s41592-019-0686-2](https://doi.org/10.1038/s41592-019-0686-2)
- Whitaker, K. E., Labbé, I., van Dokkum, P. G., et al. 2011, *ApJ*, 735, 86, doi: [10.1088/0004-637X/735/2/86](https://doi.org/10.1088/0004-637X/735/2/86)
- Wright, G. S., Wright, D., Goodson, G. B., et al. 2015, *PASP*, 127, 595, doi: [10.1086/682253](https://doi.org/10.1086/682253)
- Yung, L. Y. A., Somerville, R. S., Finkelstein, S. L., et al. 2021, *MNRAS*, 508, 2706, doi: [10.1093/mnras/stab2761](https://doi.org/10.1093/mnras/stab2761)
- Yung, L. Y. A., Somerville, R. S., Finkelstein, S. L., Popping, G., & Davé, R. 2019a, *MNRAS*, 483, 2983, doi: [10.1093/mnras/sty3241](https://doi.org/10.1093/mnras/sty3241)
- Yung, L. Y. A., Somerville, R. S., Finkelstein, S. L., et al. 2020a, *MNRAS*, 496, 4574, doi: [10.1093/mnras/staa1800](https://doi.org/10.1093/mnras/staa1800)
- Yung, L. Y. A., Somerville, R. S., Popping, G., & Finkelstein, S. L. 2020b, *MNRAS*, 494, 1002, doi: [10.1093/mnras/staa714](https://doi.org/10.1093/mnras/staa714)
- Yung, L. Y. A., Somerville, R. S., Popping, G., et al. 2019b, *MNRAS*, 490, 2855, doi: [10.1093/mnras/stz2755](https://doi.org/10.1093/mnras/stz2755)
- Yung, L. Y. A., Somerville, R. S., Ferguson, H. C., et al. 2022, *MNRAS*, 515, 5416, doi: [10.1093/mnras/stac2139](https://doi.org/10.1093/mnras/stac2139)
- Zavala, J. A., Buat, V., Casey, C. M., et al. 2022, arXiv e-prints, arXiv:2208.01816. <https://arxiv.org/abs/2208.01816>
- Zitrin, A., Labbé, I., Belli, S., et al. 2015, *ApJ*, 810, L12, doi: [10.1088/2041-8205/810/1/L12](https://doi.org/10.1088/2041-8205/810/1/L12)